

**Linear Spectroscopic Studies of Semiconductor Quantum
Wells**
by
M. W. Day

A thesis submitted to the
Faculty of the University of Colorado in partial fulfillment
of the requirements for Honors' designation for the degree of
Bachelor of Science
Department of Physics
2015

This thesis entitled:
Linear Spectroscopic Studies of Semiconductor Quantum Wells
written by M. W. Day
has been approved for the Department of Physics

Prof. Steven Cundiff

Prof. James Thompson

Prof. Judith Packer

Date _____

The final copy of this thesis has been examined by the signatories, and we find that both the content and the form meet acceptable presentation standards of scholarly work in the above mentioned discipline.

Day, M. W. (B.S.)

Linear Spectroscopic Studies of Semiconductor Quantum Wells

Thesis directed by Prof. Steven Cundiff

Manufacturing processes unintentionally introduce fluctuations in the width of semiconductor quantum wells. These fluctuations subtly modulate the optical emission energies of excitons confined within the quantum well layer. It is therefore imperative to quantify these width fluctuations so their effect on exciton confinement potentials can be accounted for in ultrafast spectroscopic studies of semiconductor quantum wells. The use of micro-photoluminescence spectroscopy makes quantifying this disorder possible. I present microphotoluminescence spectroscopy work taken in pursuit of an Honors' thesis.

Dedication

Long Dedication

Acknowledgements

Long Ack

Contents

Chapter

1	Introduction	1
2	Theory and Background	4
2.1	The Semiconductor Quantum Well	4
2.1.1	Bandgap	4
2.1.2	Confinement	7
2.1.3	The Exciton	11
2.2	Quantum Well Disorder	15
2.3	Exciton Coupling in Asymmetric Double Quantum Wells	16
2.4	Microphotoluminescence Spectroscopy	17
2.5	Photoluminescence Excitation Spectroscopy	19
3	Experimental Methods	21
3.1	The Light Source	21
3.2	Optical Components and Path Configuration for μ PL Experiments	23
3.2.1	Manufacturing the SIL	23
3.2.2	Manufacturing the Cryostat Optics Mount	25
3.2.3	Experimental Optical Path Configuration	27
3.3	μ PL Data Collection	30
3.3.1	Optical Alignment Considerations	30

3.3.2	Data Collection Process	30
3.4	Components and Optical Path Configuration for PLE Experiments	31
3.4.1	Optical Path Configuration and Alignment	31
3.4.2	Data Collection for Photoluminescence Excitation Spectroscopy	32
4	Disorder in Quantum Well Structures	34
4.1	μ PL Results and Analysis for Multiple Quantum Well Samples	34
4.1.1	Disorder in a Ten Quantum Well Structure	34
4.1.2	Disorder in a Four Quantum Well Structure	39
4.1.3	Disorder in an Interfacial Quantum Dot Structure	42
4.2	PLE Results and Analysis	44
5	Conclusion and Future Work	50
5.1	Conclusions from Linear Spectroscopic Experiments	50
5.2	Future Work	51
References		52

Figures

Figure

2.1 A typical dispersion curve minima for a direct-gap semiconductor. An optical transition is illustrated at an arbitrary value of k , where an electron is absorbing a photon resulting in a transition from the conduction band to the valance band.	7
2.2 The band structure of GaAs, the allowed states are the thick horizontal curves, and the boxed region is the direct-gap region, in which electrons can be make direct transitions across the bandgap. Note, the extrema of this region look like the dispersion curve in figure 2.1 [7].	7
2.3 A graphical representation of the one-dimensional infinite potential well of width L	8
2.4 An example of the semiconductor quantum well. These layers can be repeated arbitrarily many times.	11
2.5 A simple model for the behavior of an exciton in a quantum well, suitable for the work completed herein. The black lines correspond to the effective QW potentials for each the electron, hole, and exciton.	14

2.6 A graphical representation of the effective QW exciton potentials (black lines) and QW exciton ground states in wells of various thickness. In a), the energy of a ground state exciton located in a portion of the QW of average thickness, the blue line in b) depicts the ground state energy of an exciton located in a slightly thinner than average portion of the QW, and in c), the blue line depicts the ground state energy of an exciton located in a slightly thicker than average portion of the QW. In both b) and c), the average exciton ground state energy is depicted by the maroon dashed line.	16
2.7 A representation of a confocal optical geometry used to collect the PL from the QW sample. The PL image is being collected from a small region of the QW sample, magnified, and then collimated by the two lenses.	18
2.8 A representation of the principle of our specific μ PL experiment. The PL image leaves the SIL normal to the hemispheric surface, so it just increases n and lowers the diffraction limit.	20
3.1 A depiction of the laser cavity. The green line represents the path of our pump laser, while the red line is the Ti:Sapph beam. The birefringent filter (BRF) is rotated to select the laser wavelength.	22
3.2 A depiction of the modified mount: the actuator arm fits into a sleeve attached by a pivot to the rotating filter mount. A spring attached to both the rotating mount and aluminum block holds the sleeve to the actuator and ensures smooth rotation in either direction.	23
3.3 A depiction of the lapp. The orange casing is copper while the grey lining is lead solder. The cavity left by the ball bearing was smooth enough to polish the relatively soft ZnSe hemispheres to an optical quality finish.	24

3.4 A depiction of the polishing setup in the lathe. The off-center placement of the lapp and lapp pin allowed the lapp to rotate and move slightly to randomize the SIL polishing.	25
3.5 A representation of the optics inside the cryostat. The optics were held in place relative to each other by a gold-plated copper mounting tube, containing the lenses. This mounting tube was affixed to a mirror which directed the excitation beam into the cryostat optics and eventually the sample.	26
3.6 An exploded view of the cryostat optical components: 1. the cryostat attachment mount, 2. the cryostat mirror, 3. the copper optics tube, 4. the aspheric lens, 5 the lens retaining ring, 6. the sample and SIL retaining ring, 7. the SIL, 8. the sample, 9. the sample platform, 10. the platform retaining ring. Not rings 5. and 10. were threaded, and the SIL retaining ring clamped onto the sample platform with screws, holding the sample and SIL fixed relative to each other. There was a thin teflon ring between the asphere, the SIL, and their retaining rings to allow for limited thermal expansion and contraction of the lenses without damage.	27
3.7 A depiction of the PL spot on the spectrometer slit. The spot translates across the slit as we move the lens on the translation stage, allowing us to take vertical slices of the image as it translates across the slit.	29
3.8 A diagram of the experimental components. The second telescope was an optional feature, its use doubled the system magnification. The light pink beam represents the PL image, while the red beam represents the excitation laser.	29
3.9 A flowchart depicting the LabView code processing sequence. Each set of μ PL data was acquired using this process, where s_s was the lens step size and i_0 was the number of data collection steps to be run.	31

3.10 A diagrammatic representation of the PLE experiment. The red beam is the excitation laser while the pink beam is the PL signal. We used a long pass filter (LPF) to cut out any light with wavelength lower than 800nm, as we suspected some of the pump scatter (green) was making it to the sample, reducing our ability to control the excitation wavelength.	33
3.11 A flowchart depicting the LabView code processing sequence for the PLE experiments. Each set of PLE data was acquired using this process, where λ_{step} was the wavelength step size and i_0 was the number of data collection steps to be run.	33
4.1 A raw CCD image corresponding to one vertical slice of the PL image. In order to calculate the PL emission wavelength as a function of sample location, we found the maximum PL amplitude as a function of vertical sample position for each vertical slice.	35
4.2 A vertical 10QW PL amplitude slice at the PL maximum from a CCD raw image. Effectively, these slices were stacked together along the lens translation axis to recover the second sample location axis and build a 3D surface of either PL amplitude or PL energy.	36
4.3 A reconstructed PL image of 10QW sample surface. The small features in the image correspond to striations and dust on the surface of the sample. The excitation spot's maximum intensity occurred near the bottom of the image, corresponding to the PL amplitude maximum.	37
4.4 A μ PL energy deviation image for the 10QW sample. Note the energy deviation was found to be 0.1meV, peak to peak, at maximum.	38
4.5 A reconstructed image of the PL amplitude of the 4QW sample.	41

4.6 An energy deviation map for the 4QW sample. Note the large-scale feature across the middle of the sample. This most likely corresponded to a scratch across the sample which slightly deformed all four wells below it, so we see an energy signature of this deformation.	41
4.7 An energy deviation map for the IQD sample. The energy deviations in the IQD sample are much larger than those measured in the 4QW and 10QW samples, even though the IQD structure is periodic and suffers from similar spectral averaging to the other samples. The white blemish is an anomalous noise spike.	43
4.8 An example PLE spectrum taken on a 10nm barrier AQW sample. We were able to monitor the emission from both wells as a function of excitation frequency, which allowed us to simultaneously quantify emission from one well due to resonant excitation and emission from the adjacent well due to coupling. The lower energy vertical trace corresponds to emission from the wide well while the higher energy trace corresponds to emission from the narrow well. The white diagonal line is laser scatter, and represents locations of equal excitation and detection frequencies.	46
4.9 A close-up of the coupling cross-peaks. The green, dashed circle corresponds to a coupling peak between wells in the Stokes direction: the narrow well absorbs the laser excitation, while the wide wells emit a portion of the absorbed energy. The orange, dashed circle corresponds to a coupling peak in the anti-Stokes direction: the wide well absorbs and the narrow well emits a portion of the excitation energy. The magenta circle corresponds to resonant excitation in the narrow well, and the turquoise circle corresponds to resonant excitation in the wide well. The diagonal white trace is the laser scatter.	47

4.10 A set of three PLE vertical profiles taken at the wavelength of peak emission intensity for a) the 30nm, b) the 10nm, and c) the 5nm barrier width AQW. Note: the narrow well emission intensity was much lower than the wide well emission intensity, and was scaled up for graphical comparison. For each sample, the most intense peaks correspond to resonant excitation and absorption. The coupling intensity can be measured by looking at the intensity of the cross peaks, represented by the slightly smaller peaks under each of the resonant excitation peaks.	48
4.11 Temperature dependance for the PLE coupling peaks for barrier width of a) 30nm, b) 10nm, and c) 5nm. The top plots are un-normalized coupling peak intensities, while in the bottom plots, the cross-peak intensity is normalized to the resonant peak intensity. The coupling intensity seems to peak have a temperature peak for the 30nm and 10nm barrier samples. The coupling peak intensities in both the normalized and unnormalized plots for these two samples decrease as sample temperature increases, suggesting that coupling is temperature mediated. However, in the 5nm barrier, there seems to be little temperature dependance of coupling intensity in the normalized plot. . . .	49

Chapter 1

Introduction

Nanoscale semiconductor manufacturing techniques allow for the realization of unique nanostructures ideally suited for a broad range of optical and electronic devices. Precise control of material geometry and immense parametric freedom during device fabrication makes tailoring semiconductor nanostructures to their applications relatively easy. With these processes, confining charge carriers on the scale of their de Broglie wavelengths becomes possible. Nanostructures employing confinement on such small scales have proven to be especially useful. A subset of these structures, known as quantum wells, confine their charge carriers in just one dimension. It is therefore possible to create devices like highly efficient photo- and laser diodes. Additionally quantum wells (QWs) have shown particular promise as low noise transistors, and as saturable absorbers in mode-locked lasers, among other uses. In addition to their applications, QWs have proven useful as a testbed for studying the quantum interactions between light and matter [6, 7].

Despite immense progress in the growth of QWs, manufacturing processes still unintentionally introduce inhomogeneities to the layer thickness during crystal deposition. This translates to an uneven interface between two different materials on the scale of a few crystal monolayers. For a quantum well structure, small fluctuations in interface flatness translate to small fluctuations in well width as these happen at both interfaces of the quantum well and barrier layers. These small width fluctuations are a form of structural disorder.

Disorder affects charge carrier mobility within QWs, which can affect device efficiency

and optical activity. Because of the ubiquity of QW structures, it is important to characterize disorder. Being able to quantitatively map structural disorder within QWs can help manufacturers improve the uniformity of their QWs, and in turn the quality and efficiency of their devices. For use of QWs in optical experiments, quantifying the spatial distribution of disorder is important because complete information concerning inhomogeneous contributions to the overall spectral response can help us enrich our understanding of many-body exciton interactions.

The local thickness of a QW structure can be optically determined: simply by spectrally resolving the total emission signal from a photo-excited QW, allows one to determine the average thickness of a QW layer [9]. Structural QW disorder modifies the thickness of wells and therefore slightly modulates the energies of quantum well exciton states as a function of position within the well. Therefore, disorder can be experimentally quantified. By obtaining a spatial map of QW emission energies with sufficient resolution spatial and spectral resolution, we can determine the local well thickness and therefore obtain a quantitative picture of disorder within a QW. To do this, we optically excite a QW sample and spectrally imaging the emitted light, a linear spectroscopic technique known as micro-photoluminescence spectroscopy. Doing so, we recover a spatially resolved map of emission energies, and thereby quantify QW structural disorder [23].

In addition to studying quantum well disorder, linear spectroscopy is useful for characterizing the energy profile of electron states in matter. For example, we can use linear spectroscopy to study exciton states and incoherent coupling in the asymmetric double quantum well (AQW). Due to the geometrically tunable of AQW structures, these systems are great testbeds for various quantum coupling phenomena, and understanding incoherent coupling between exciton states in asymmetric double quantum wells allows us to fulfill two important experimental goals: we obtain a better understanding of the exact absorption energies of the various exciton states, and we can explore incoherent coupling mechanisms between exciton states in each of the wells. In particular, we can explore the temperature and barrier width

dependence of coupling between exciton states in AQW samples.

In this thesis, I present the development of a high-resolution micro-photoluminescence spectroscopy (μ -PL) experiment to quantify QW disorder. Furthermore, I employ this experiment to produce a quantitative measurement of disorder on three different types of QW structures: a periodic ten-quantum well structure, a periodic four-quantum well structure, and an interfacial quantum dot ensemble. In addition to μ -PL experiments, I present the development of photoluminescence excitation spectroscopy (PLE) to study the incoherent coupling between exciton states in Gallium Arsenide/Indium Gallium Arsenide AQW structures. I will then use our PLE characterization of exciton states in AQWs to comment on and add to the relative paucity of information on thermal and barrier width mediation of coupling between exciton states in the stokes and anti-stokes directions.

This thesis is structured such that Chapter 2 is a theoretical introduction to the physical concepts necessary to understand our μ -PL and PLE experiments. Chapter 3 will be a description of our experimental methods, while results of our experiments will be presented in Chapter 4. Chapter 5 will conclude this thesis with our experimental interpretations and a discussion of possible experimental directions for the future.

Chapter 2

Theory and Background

In this chapter, I will provide the theoretical background necessary to understand the work presented in this thesis. The first section will deal with the definition and importance of the bandgap of a material, the second will introduce the effects of confinement on electrons within semiconductors, leading to a discussion of charge carrier confinement within semiconductor quantum wells. The third section will introduce the concept of semiconductor quantum well disorder, and the fourth will motivate the study of semiconductor quantum well disorder with micro photoluminescence spectroscopy. Finally, I will discuss the optical properties of asymmetric double quantum wells and how to use photoluminescence excitation spectroscopy to investigate incoherent coupling between excitons in asymmetric double quantum wells.

2.1 The Semiconductor Quantum Well

2.1.1 Bandgap

In order to understand how electrons behave in a crystalline solid, one must first understand how bound electrons act when arbitrarily many atoms are brought together in a lattice structure. Consider a collection of N atoms sufficiently far apart such that interactions between atoms can be neglected. In this limit, electrons in an atom occupy discrete energy levels. For instance: suppose all N of our atoms are monatomic hydrogen atoms. In our

system, an electron behaves according to the following Hamiltonian:

$$\hat{H} = -\frac{\hbar^2}{2m} \nabla^2 - \frac{e^2}{2\pi\epsilon_0 r}. \quad (2.1)$$

We can find the electron wavefunctions $\psi(x)$ by solving the time independent Shrödinger equation,

$$\hat{H}\psi(x) = E_n\psi(x) \quad (2.2)$$

where E_n is the energy of the n^{th} energy level. This equation can be solved using the usual methods [11], but doing so here would be a diversion, so here are the crucial points: evidently, the $n = 1$ ground state electron wavefunction (again neglecting interactions between atoms and ground state perturbations) is

$$\psi(r) = \frac{1}{\sqrt{\pi a_0^3}} \exp\left(-\frac{r}{a_0}\right) \quad (2.3)$$

where a_0 is the Bohr radius. Note: each $n = 2$ energy level in this system is N -fold degenerate, as there are N orbitals with the same energy. Considering just the $n = 1$ states and neglecting perturbations, electrons in these states evidently all have energy

$$E_1 = -13.6\text{eV}. \quad (2.4)$$

In the limit that many atoms are brought together such that interactions can no longer be neglected, two things happen: each N -fold degenerate electron energy level will split into N components, and these levels will become so close that they will smear into allowed and disallowed energy densities of state [13, 18, 11, 7, 8]. Roughly speaking, the occupied states are known as the “valance band” states, and the unoccupied states are known as the “conduction band states”. The energy difference between the valance band and conduction band is called the bandgap, and its importance will be illuminated momentarily.

These band states are simultaneous eigenstates of both the Hamiltonian and the crystal momentum [7, 8]. This means that bands can be easily depicted in momentum space using dispersion curves. Dispersion curves map out allowed band energies in momentum space,

and their full functional shape is dependent on the types and arrangement of constituent atoms. Solids can be broadly organized into three categories based upon the momentum space (or k-space) arrangement of their electron bands and the location of their chemical potential. Crucially, in semiconductors, the bandgap is roughly 1eV and can therefore be optically accessed [8].

Sometimes, as in the case of Gallium Arsenide (GaAS) structures, a local valance band minima and conduction band maxima occur for the same value of k in k-space. Semiconductors with this sort of bandstructure are known as direct-gap semiconductors. Around this value of k , electrons can absorb a photon with enough energy to undergo a direct transition from the valance band to the conduction band [13, 15]. This fact forms the basis of linear and nonlinear optical studies of semiconductor nanostructures [6] and the operating principle of various photonic devices.

A slight complication to this picture is that there are two valance band curves around this value of k in GaAs, as seen at the gamma point in Figure 2.2. The holes which occupy the valance band energies of less curvature are known as “heavy holes” while the holes which occupy the valance band energies of greater curvature are known as “light holes”. “Heavy” and “light” refer to the relative effective masses of particles occupying these states. It is the heavy holes that dominate the long-timescale physics we are interested in, so we can ignore the effect of light holes here.

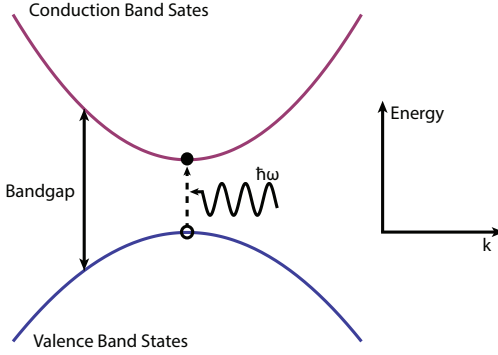


Figure 2.1: A typical dispersion curve minima for a direct-gap semiconductor. An optical transition is illustrated at an arbitrary value of k , where an electron is absorbing a photon resulting in a transition from the conduction band to the valance band.

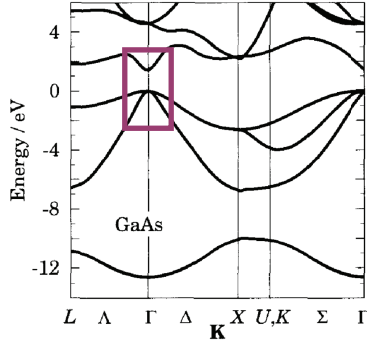


Figure 2.2: The band structure of GaAs, the allowed states are the thick horizontal curves, and the boxed region is the direct-gap region, in which electrons can make direct transitions across the bandgap. Note, the extrema of this region look like the dispersion curve in figure 2.1 [7].

2.1.2 Confinement

It is well known that nanometer scale confinement of particles results in quantized energy states [11]. In the previous section, I briefly introduced the bandgap, and its important physical properties. In this section, I'll illustrate an interesting application of band theory: the semiconductor quantum well (QW). First, it is important to understand what we mean

by confinement, and how quantized energy levels arise for confined particles. I will draw an analogy to a familiar physical situation, the particle confined within an infinite potential. I will then use this analogy to construct a physical picture for QWs, and then I will discuss the formation of excitons and a simple physical model of their behavior, sufficient for understanding the spectroscopy conducted herein.

Perhaps the simplest problem in quantum mechanics is the of confinement of a particle in an infinite, one dimensional potential well. I will sketch a derivation of the wave function of a particle trapped in such a well, and use this derivation as the basis for exploring the physics of the QW exciton. We will begin by considering an arbitrary particle confined in a one dimensional infinite potential well. The potential that our arbitrary particle feels is:

$$V(x) = \begin{cases} 0 & 0 < x < L \\ \infty & x < 0, x > L \end{cases}$$

where L is the length of the potential well. Graphically, the potential the particle feels looks like Figure 2.3.

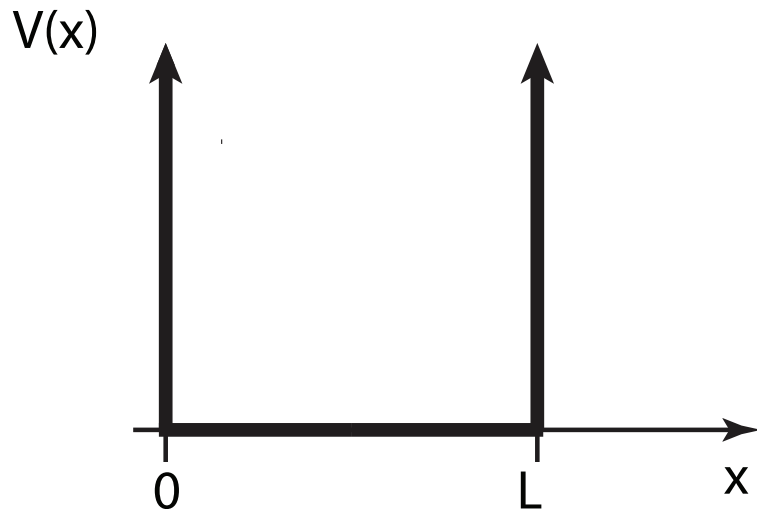


Figure 2.3: A graphical representation of the one-dimensional infinite potential well of width L .

Our task is to solve the time independent Schrödinger equation to show how quantized bound states arise for one-dimensional confinement. The time independent Schrödinger equation reads:

$$\hat{H}\psi(x) = E\psi(x) \quad (2.5)$$

where E is the energy of the particle, and $\psi(x)$ is the particle's wavefunction. The particle will evidently be confined to exist in the well, so our Hamiltonian inside the well is just

$$\hat{H} = -\frac{\hbar^2}{2m} \frac{\partial^2}{\partial x^2} \quad (2.6)$$

where m is the particle's mass, and E is the particle's total energy. The time independent Schrödinger equation now reads:

$$\frac{\partial^2}{\partial x^2}\psi(x) = -\alpha\psi(x) \quad (2.7)$$

where we define

$$\alpha = \frac{2mE}{\hbar^2}. \quad (2.8)$$

Because the wave function must be continuous at $x = L$ and $x = 0$, i.e. it vanishes at those locations, and the potential is odd about the origin, solutions to eq. 2.7 have the form:

$$\psi(x) = A\sin(kx) \quad (2.9)$$

where k contains E and is determined by our boundary conditions. Now we want $\psi(L)$ to vanish, but we can't have $A = 0$, because that is the trivial solution to eq. 2.7. Therefore, because we want $\psi(L) = A\sin(kL) = 0$, we must have $ka = \pm n\pi$ where $n \in \mathbb{N}$. Now, we can absorb all of the negative combinations of kL into our normalization constant, A , and we have, then, that

$$k_n L = n\pi \quad (2.10)$$

where the subscript denotes the fact that we now have infinitely many, *discrete* solutions to eq. 2.5. Evidently

$$k_n = \frac{n\pi}{L} \quad (2.11)$$

and therefore

$$\psi(x) = A \sin\left(\frac{n\pi x}{L}\right). \quad (2.12)$$

The boundary condition at $x = L$ sets our value of k , and if we plug in eq. 2.9 to eq. 2.7, then we have $k_n^2 = \alpha$. Now, the allowed energies in the well are

$$E = \frac{n^2\pi^2\hbar^2}{2mL^2}. \quad (2.13)$$

It will do us no good to normalize the wavefunctions we found, as their use for our purposes is minimal. The important part is that confinement in one dimension resulted in our particle occupying *discrete* energy levels whose energy depends on the physical size of the confinement potential.

Using layers of semiconductors, one can generate similar one-dimensional confinement effects for electrons. A simple way this can be done is by sandwiching a layer of low-bandgap semiconductor material in between two layers of higher bandgap materials [7]. One period of this structure is shown in Figure 2.4. If the well material is a direct-gap semiconductor, then simple optical transitions (i.e. not mediated by phonons) across the bandgap can be made, as the transition illustrated in Figure 2.1. Figure 2.2 is the band structure for GaAs, the chosen well material for the studies of growth disorder. Annotated on the figure is the direct-gap transition zone of interest. The potential well created by the semiconductor sandwich leads to quantization of electron states within the well layer [14, 7, 6]. We can access each of these states optically, making the QW a great testbed for exploring electron dynamics within a simple and well-known potential [6].

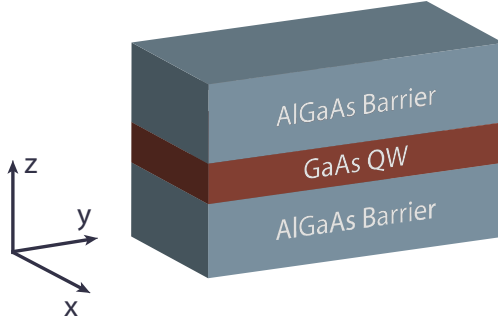


Figure 2.4: An example of the semiconductor quantum well. These layers can be repeated arbitrarily many times.

2.1.3 The Exciton

The simple picture presented above does not quite adequately represent the physics of an electron within a quantum well, however. After an excited electron transitions from the valence band to the conduction band, it will leave behind a vacancy, or “hole” [14, 7]. The electron feels a screened Coulomb potential from this vacancy, as the vacancy is positively charged. I’ll briefly sketch why this potential arises and then introduce the key concept of this section: the exciton. Imagine a number of electrons have been excited within the QW. Now, spatially, one will have a quasi-neutral distribution of electrons and holes in the well layer: an electron-hole plasma. I will assume that the holes are stationary relative to the electrons in the well, and that the excitation density is relatively low. These assumptions are *a priori* unphysical, but they immensely simplify the derivation of the electric potential QW electrons feel while preserving the key physics.

Let’s explore the local behavior of an excited electron due to a single adjacent hole in the QW. Note that in this picture, electrons everywhere in the QW feel a Coulomb attraction to the hole, but the electrons adjacent to the hole screen its effects from charges far away. This phenomenon, known in plasma physics as Debye shielding [5] and in quantum mechanics as electron screening [11], modifies the pure Coulomb potential one would expect a single

electron-hole pair to experience.

We will assume that the electrons in our electron-hole plasma obey a Maxwellian density distribution, as we are concerned with only long-timescale behavior. Now, the local density of electrons around the hole is

$$n_e = n_0 \exp\left[\frac{e\phi}{kT}\right] \quad (2.14)$$

where n_0 is the electron density far away, e is the electron charge, ϕ is the local electromagnetic potential, and T is the electron temperature. A complete derivation for this electron number density in an arbitrary plasma can be found in [5]. This is the local electron distribution, and we can assume $e\phi \ll kT$ because the potential an electron feels due to one hole can be considered small relative to its thermal energy, even at low temperatures. Taylor expanding to first order, we find that

$$n_e \approx n_0 \left[\frac{e\phi}{kT} \right]. \quad (2.15)$$

Now, our local charge density is

$$\rho(r) = e \left[\delta(r) - n_0 \left(\frac{e\phi}{kT} \right) \right] \quad (2.16)$$

where we've assumed that the hole has positive charge magnitude e , is infinitely small, and situated at the origin. In order to figure out what ϕ is, we must solve the Poisson equation, assuming quasi static conditions:

$$\nabla^2 \phi(r) = -\frac{\rho(r)}{\epsilon_0} \quad (2.17)$$

For our charge density, the Poisson equation reads

$$\epsilon_0 \nabla^2 \phi(r) = -e \left[\delta(r) + n_0 \left(\frac{e\phi}{kT} \right) \right]. \quad (2.18)$$

We can define a constant,

$$k^2 = \frac{n_0 e \phi}{\epsilon_0 k T} \quad (2.19)$$

and now the Poisson equation is

$$(\nabla^2 - k^2)\phi = -\frac{e\delta(r)}{\epsilon_0}. \quad (2.20)$$

This is known as the screened Poisson equation, and its solution is

$$\phi(r) = -\frac{e}{4\pi\epsilon_0 r} e^{-kr}. \quad (2.21)$$

Now, $\phi(r)$, functionally, the correct result (albeit with a different k) had we proceeded under the more rigorous Thomas-Fermi approximation, assuming only that the potential is weak and variations are slow and smooth over a distance around the hole equivalent to the inverse of the Thomas-Fermi wavevector. This turns out to be a very good approximation for the local potential an electron feels relatively close to a hole in a solid [16]. The single-particle hamiltonian for an electron in the QW is now:

$$\hat{H} = -\frac{\hbar^2}{2m} \frac{\partial^2}{\partial x^2} - \frac{e}{4\pi\epsilon_0 r} e^{-k_0 r} \quad (2.22)$$

where $k_0^2 = \frac{n_0 e \phi}{k T_f}$ is the “corrected” k for the same potential derived under the Thomas-Fermi approximation [16].

Note that if the potential electrons feel was exactly Coulombic in nature, then any bound state between an electron and a hole would be hydrogenic [11]. This potential, however, is *not* exactly Culombic in nature, so the bound states between the electrons and holes can't be described by hydrogenic wavefunctions. Nevertheless, bound states between an exited electron and an adjacent hole do exist, and when an electron and hole occupy these states, they form a quasiparticle called an “exciton”, and they can be treated as a single particle with an effective mass [13, 7].

The subtleties of the exciton wave function are treated in [13], exploring their exact functional form and corresponding density of exciton states in the QW will not be of use to us here. Only energy levels of the QW exciton are discretized by its confinement, those of excitons created in the bulk are not. A final important note: in my derivation, the hole is

assumed to be a stationary point particle. This is emphatically not true, but the physics doesn't change that much if we assume both charge carriers are mobile. Excitons can still be treated as a single particle even after removing this assumption. Figure 2.5 depicts a simple physical picture for excitons: the electron and hole excited energy levels can be thought of as the ground state of a particle trapped in a finite potential.

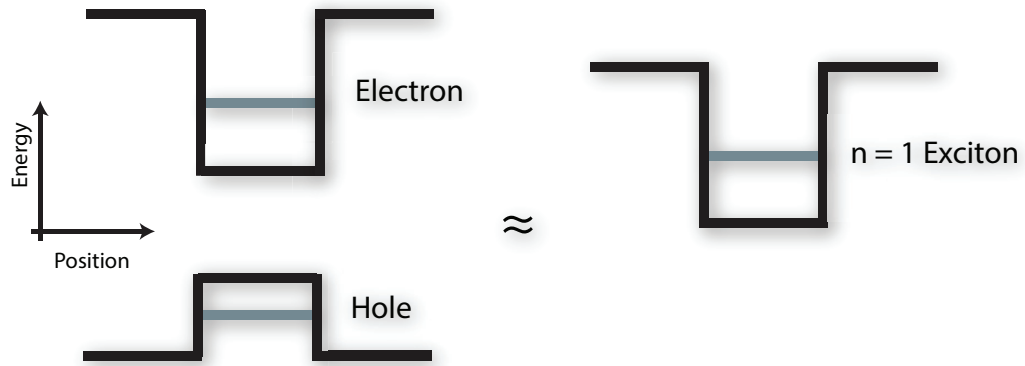


Figure 2.5: A simple model for the behavior of an exciton in a quantum well, suitable for the work completed herein. The black lines correspond to the effective QW potentials for each the electron, hole, and exciton.

2.2 Quantum Well Disorder

When an exciton is created, in a direct gap semiconductor such as GaAs, the charge carriers can recombine from either exciton “ground” state ($n = 1$), or “excited” states ($n > 1$) and emit a photon equivalent to the bandgap energy less the exciton binding energy [9]:

$$E_{emit} = E_{gap} - E_{bind}. \quad (2.23)$$

Since I am interested in linear, long-timescale exciton physics, we can treat QW excitons as an approximately two-level system, only looking at ground state recombination. The emission energies of QW excitons will be dependent on well depth, a function of the barrier composition and well width. The light emitted as a result of carrier recombination after optical excitation is called photoluminescence (PL). Additionally, because the binding energy is small, we cool our samples to low temperature to study exciton PL.

Control of QW layer thickness has improved immensely, as QW structures can be made to precise specifications with modern molecular beam epitaxy [7]. However, imperfections of layer width on the order of a crystal monolayer occur unavoidably at the interface between the well and barrier materials during the QW manufacturing process [22, 21, 10]. These defects, a form of structural disorder, slightly change the width of the well layer and thus subtly modulate exciton emission energies, an illustration of which is shown in Figure 2.6. By analogy to eq. 2.11, excitons localized in slightly thinner than average sections of the QW will emit at slightly higher energies than average. Conversely, excitons localized in thicker than average sections of the QW will emit at slightly lower energies than average. Thus, structural disorder is the main contribution to inhomogeneous broadening in the QW coherent optical response [4].

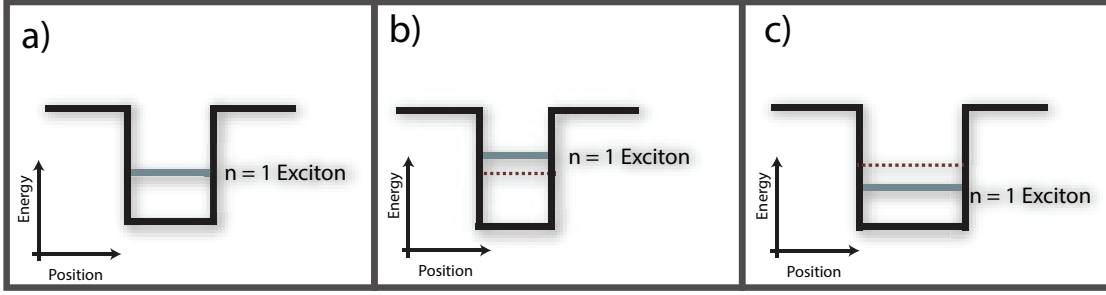


Figure 2.6: A graphical representation of the effective QW exciton potentials (black lines) and QW exciton ground states in wells of various thickness. In a), the energy of a ground state exciton located in a portion of the QW of average thickness, the blue line in b) depicts the ground state energy of an exciton located in a slightly thinner than average portion of the QW, and in c), the blue line depicts the ground state energy of an exciton located in a slightly thicker than average portion of the QW. In both b) and c), the average exciton ground state energy is depicted by the maroon dashed line.

2.3 Exciton Coupling in Asymmetric Double Quantum Wells

Quantum coupling between excitons occurs when multiple quantum wells get close enough so that the exciton wavefunction can tunnel slightly into adjacent wells [11, 7]. In order to study quantum coupling between states in adjacent QWs, however, it is not simply enough to grow multiple quantum well layers fairly close to one another. Evidently, if each of the wells is of identical thickness, then QW PL from one well will be spectrally indistinguishable from another. Indeed, it is necessary to grow wells of varying thickness when studying coupling in multiple quantum wells [12].

Asymmetric multiple quantum well (AQW) samples are a convenient system in which to study exciton coupling between wells. Incoherent (long timescale) coupling between exciton states can occur through dipole-dipole interactions [19], thermal activation [?] or other incoherent processes. When excitons absorb light resonant to the narrow well (NW) exciton ground state and emit light resonant to the wide well (WW) exciton ground state, then the

coupling between those two wells happened in the Stokes direction. Anti-Stokes coupling is just the reverse of this process: WW absorption and NW emission. In other words, if we see PL peaks that correspond to absorption in one well and emission from the other well, we can quantify the intensity of that coupling. Understanding incoherent coupling between excitons in AQWs is of interest because an improved understanding of the various processes that govern carrier transfer in nanostructures can help improve the efficiency and quality of nanostructure devices like photodiodes and transistors. Additionally, an increased understanding of exciton coupling processes is of fundamental research interest.

2.4 Microphotoluminescence Spectroscopy

Because local QW thickness determines exciton emission energy, a spatial picture of disorder is possible through spectral imaging. By using a continuous wave (CW) excitation source to create a population of QW excitons and monitoring the emission energy as a function of sample position, one can extract the local QW width [4]. With sufficiently high resolution, obtaining a map of emission energies for a representative portion of a QW sample is possible. In order to obtain a map of emission energies, one must monitor the photoluminescence (PL) energies as a function of position. In a PL experiment, excitation light is directed upon a sample, exciting a large number of charge carriers to the conduction band. In a PL experiment on a QW, we create a large number of excitons, and when they recombine, they emit a photon. If we regard the exciton as a two level system, by exciting QW excitons near-resonantly, the PL energy will be a function of local well width. The key point is this: by obtaining a spatial PL signal, and then resolving the PL energy at each location, we obtain a measure of local QW width and therefore structural disorder.

In order to obtain an image of PL, we must collect the signal carefully. More precisely, if we are to obtain a spatial picture of QW disorder, we must collect and spectrally resolve a PL image. The PL will be emitted from the exciton population over a 4π solid angle, so we must construct an imaging system and place the QW directly at the focus to obtain a

clear PL image. Furthermore, since the scale of the disorder is on the order of 100nm [22], we must have comparable resolution for the PL image. A system capable of resolving a PL image is shown in Figure 2.7. The magnification of the PL image is set by the ratio of the lens focal lengths. Namely:

$$M = \frac{f_1}{f_2} \quad (2.24)$$

where f_2 and f_1 are the focal lengths of the short focal length lens and the long focal length lens respectively, and M is the image magnification factor. A PL experiment with sub-micron resolution which is capable of spectrally resolving a PL image is known as a “microphotoluminescence spectroscopy” experiment, or μ PL.

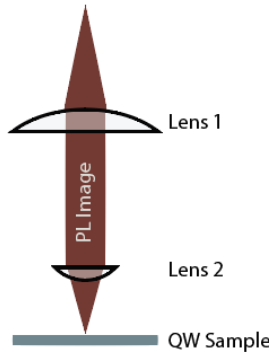


Figure 2.7: A representation of a confocal optical geometry used to collect the PL from the QW sample. The PL image is being collected from a small region of the QW sample, magnified, and then collimated by the two lenses.

As simple as the PL image collection is, it is difficult to obtain the requisite image resolution because the PL is around 750-800nm wavelength, but as asserted above, the islands can be smaller than this. The Abbe diffraction limit is

$$d = \frac{\lambda}{2nNA} \quad (2.25)$$

where λ is the wavelength of the PL image, n is the index of refraction in the intermediate

space between the sample and lens 2 (the imaging lens) in Figure 2.7, and NA is the numerical aperture of lens 2. Note that $NA = f/D$ where f is the focal length of the imaging lens and D is its diameter. In our case, $d \approx 500\text{nm}$ for $\lambda \approx 780\text{nm}$, $n = 1$ in vacuum, and $NA = 0.83$, as that was the NA of the lens in our experimental setup. Even if we were able to operate our imaging system at the Abbe diffraction limit, we still wouldn't have the resolution necessary to resolve adjacent disorder sites.

In order to get around this limit, we either need to resort to exotic microscopic techniques, or we can employ a fairly simple trick. It has been shown that by increasing the index of refraction (n) with a solid immersion lens (SIL), the Abbe diffraction limit can be substantially reduced [23] paper, and broad SIL paper. In order to do this, one simply places a hemisphere of sufficiently high n material between the sample and the imaging lens. Figure 2.8 is a diagrammatic representation of this improvement. Note, I'll use SIL and hemisphere interchangeably from here on out, though they aren't necessarily interchangeable, as "SIL" refers to type of lens, generally a truncated sphere of some degree.

In my experimental setup, I used a Zinc Selenide (ZnSe) SIL, for which $n = 2.4$ at $\lambda = 780\text{nm}$. This improvement decreases the diffraction limit from $d \approx 500\text{nm}$ to $d \approx 185\text{nm}$, roughly sufficient resolution for our purposes. I'll expand on the precise setup in the next chapter, but the experiment will be very similar to what I've just described.

2.5 Photoluminescence Excitation Spectroscopy

Photoluminescence Excitation spectroscopy (PLE), a linear technique, can provide information on the energies and locations of various exciton states in AQWs. PLE is a simpler method than μ PL, as only the relative PL intensity is monitored. Generally, one monitors PL at a specific detection wavelength as the excitation wavelength is scanned across a wide range. By monitoring the PL as a function of excitation wavelength, we obtain a measure of absorption by the sample [8]. By extending this technique slightly, we can quantify the coupling between excitons in AQW samples. In order to do this, we scan the

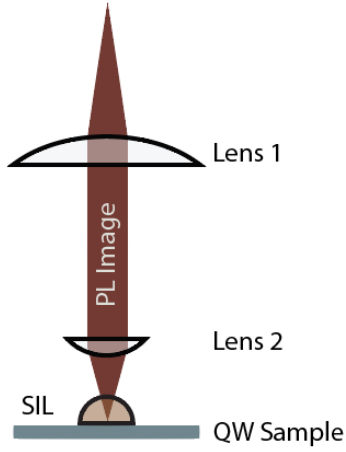


Figure 2.8: A representation of the principle of our specific μ PL experiment. The PL image leaves the SIL normal to the hemispheric surface, so it just increases n and lowers the diffraction limit.

excitation wavelength of our light source, and take a PL spectrum (not just a single intensity value) for each different excitation wavelength. That way, the emission from both wells can be monitored as a function of excitation wavelength, and coupling between two wells can be quantified: as the excitation wavelength scans over an exciton resonance in one well, the PL signal from the other well can be monitored to see if that resonant excitation at one energy increases PL at the other.

Chapter 3

Experimental Methods

In this chapter I will describe the experiments I conducted for this thesis. The first section will deal cover the configuration and customization of the continuous wave (CW) Titanium Sapphire laser I used as an excitation source for conducting both PLE and μ PL experiments. Section two will cover the design and construction of the in-cryostat optic mount for the μ PL experiment as well as the optical configuration for data collection. Section three will illustrate the data collection procedure used in μ PL experiments, as well as the function and implementation of LabView code I wrote for hardware control and data acquisition. In section four, I will lay out the optical design of our PLE experiments and in section five, I will discuss the experimental data collection process and signal optimization routines.

3.1 The Light Source

The PLE and μ PL experiments required a stable CW laser light source with fairly high-power and narrow line-width. For μ PL, it was important that we have a fairly Gaussian and symmetric beam so we could obtain the desired spot-size and resolution at the sample. Additionally, conducting PLE scans required that we have the ability to computer control the laser wavelength over a range of wavelengths, roughly a spectral region from $\lambda = 780\text{nm}$ to $\lambda = 850\text{nm}$. The laser we used for this task was a Schwartz Electro Optics Titan-CW Titanium Sapphire (Ti:Sapph) laser. Its specifications were fairly close to our needs, as its

specified operating power is 500mW with a tunable range from roughly 700-820nm [20].

The laser cavity can be configured for either CW or pulsed operation. In CW operation a 532nm pump beam, 5W of power, enters the cavity through a series of steering mirrors. After entering, the pump passes through a lens to focus the pump on the Ti:Sapph crystal. When the beam leave the gain medium, the remaining pump light passes through the end mirror and terminates at the back of the laser enclosure. The laser configuration is shown in Figure 3.1.

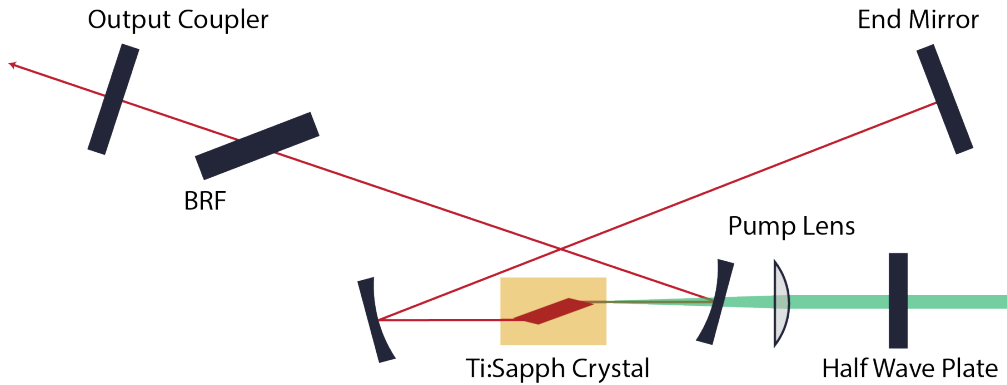


Figure 3.1: A depiction of the laser cavity. The green line represents the path of our pump laser, while the red line is the Ti:Sapph beam. The birefringent filter (BRF) is rotated to select the laser wavelength.

Though the Ti:Sapph laser nearly met our specifications, it required two modifications to be operable in our experiments. First, we needed to add a computer controlled actuator to rotate the the birefringent tuner in order to allow for increased tunability and repeatability relative to the original manually actuated micrometer. We modified the rotation mount for the birefringent filter (BRF) to accommodate a Newport TRB25 linear actuator. The linear actuator pushed a spring-loaded arm to rotate the BRF to a specified angle and select our desired wavelength. Figure 3.2 depicts the modified BRF mount with the actuator attached.

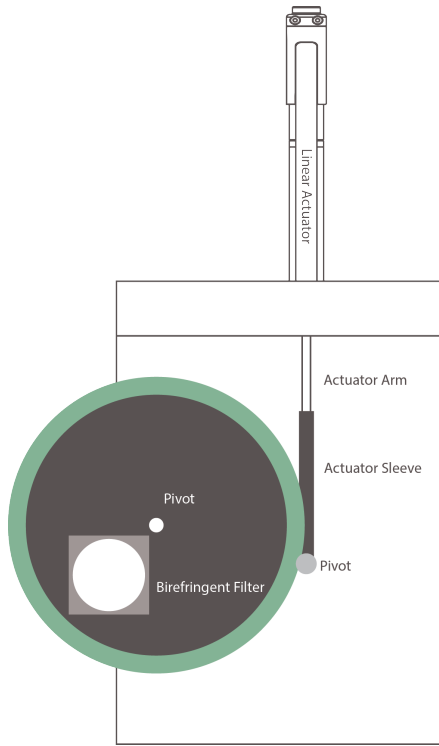


Figure 3.2: A depiction of the modified mount: the actuator arm fits into a sleeve attached by a pivot to the rotating filter mount. A spring attached to both the rotating mount and aluminum block holds the sleeve to the actuator and ensures smooth rotation in either direction.

3.2 Optical Components and Path Configuration for μ PL Experiments

3.2.1 Manufacturing the SIL

In order to obtain the resolution necessary to image disorder, the experiment employed a solid immersion lens (SIL) at the surface of the sample to increase the index of refraction at the imaging plane. I chose ZnSe as the SIL material, as its index of refraction at 780nm is $n=2.53$ [1], high enough to give us a diffraction limit near the disorder feature size. However, ZnSe SILs are not commercially available, so we resorted to manufacturing SILs from a stock ZnSe window. The window measured 2.54cm diameter by 1cm thickness, and our goal was to manufacture SILs of roughly 3mm in radius. To begin, we used a core drill, diameter

6.35mm, to cut out a cylindrical chunk of ZnSe. We then centered and glued the cylindrical stock material to a brass dowel, 2mm in radius. After the ZnSe was glued to the rod, the SIL shaping began. We put the brass dowel in a power drill and used 220 grit sandpaper to shape the ZnSe cylinder roughly into a hemisphere.

When the SIL was in the roughly correct shape, we lapped and polished the hemispherical surface until the SIL was the correct size. Additionally, since the experiment required optical quality surfaces, this was a careful and fairly lengthy process. I made the polishing lapps by machining a 2.54cm diameter copper rod to roughly 2cm in diameter with a 1.8cm wide by 1cm deep cavity. Then, I melted lead solder into the cavity, let it harden, and machined the face of the copper and solder until they were flush and machine-smooth. Then, I pressed a cleaned, 6.35mm diameter ball bearing halfway into the solder. Figure 3.3 depicts what a finished lapp looked like before it was used to grind and polish the SIL.

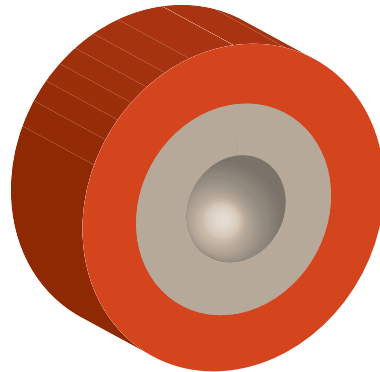


Figure 3.3: A depiction of the lapp. The orange casing is copper while the grey lining is lead solder. The cavity left by the ball bearing was smooth enough to polish the relatively soft ZnSe hemispheres to an optical quality finish.

After the lapp was made, we mounted the dowel with the SIL attached to a glass-working lathe. As the lathe rotated, we placed the lapp with a mixture of diamond polishing solution and mineral oil onto the SIL and held it in place with a sharpened wire. The wire and Lapp were set off-center relative to the SIL so the friction of the rotating SIL would

randomly move the lapp so as to evenly polish the surface of the hemisphere. A depiction of this setup is in figure 3.4. We iterated polishing runs, changing the lapp each time we stepped down in grit size (from $10\mu\text{m}$ to $5\mu\text{m}$ to $1\mu\text{m}$). We then polished the hemisphere in a new lapp filled with $0.3\mu\text{m}$ colloidal silica polishing solution. After the polishing process finished, the SIL was removed from the dowel and the flat surface was polished on a flat lapp with colloidal silicon mixture. When the process finished, we had a hemispherical (to within 1%) ZnSe SIL.

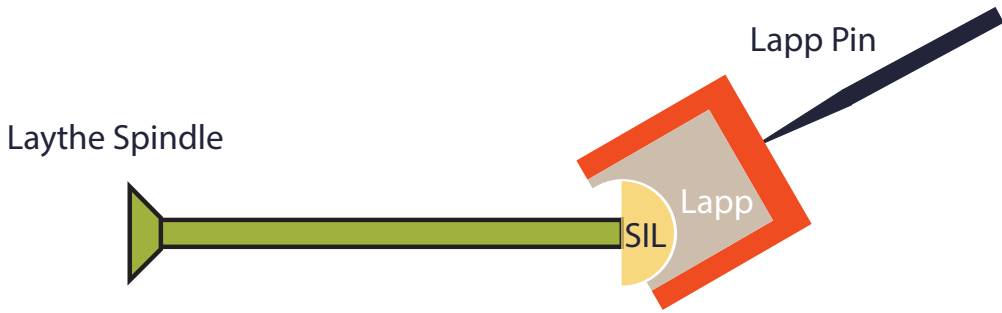


Figure 3.4: A depiction of the polishing setup in the lathe. The off-center placement of the lapp and lapp pin allowed the lapp to rotate and move slightly to randomize the SIL polishing.

3.2.2 Manufacturing the Cryostat Optics Mount

In order to achieve the desired imaging resolution, our chosen optical geometry (refer to Figure 2.4) required a high-NA lens as the imaging lens. We therefore chose an Edmund Optics $0.83NA$, 9mm effective focal length aspheric lens. Together with our ZnSe SIL, this gave us an Abbe diffraction limit of $d = 185.05\text{nm}$ for PL centered around $\lambda = 780\text{nm}$. This diffraction limit is less than our goal of $d = 200\text{nm}$. As our experiment required cooling to cryogenic temperatures, we had to build a mechanically and thermally stable optics platform to hold the lenses and QW sample together in the correct configuration. Therefore, working with our machinists, I designed an optics mount to hold the in-cryostat optical components

which are seen in Figure 3.6. The optics mount stands vertically in our Cryo-Con 8CN bath cryostat. Therefore, since the excitation laser enters the cryostat vertically, we designed the optics mount to be held to a mirror which filled the entire optics mount and was positioned at a 45 degree angle so as to direct the laser to the sample and capture the total PL image. The mirror was ground by taking a stock Thor Labs 2.54cm diameter mirror, protecting the silvered face with weak glass tape, cutting the mirror to 3mm thick, and securing the mirror to an aluminum rod of 15mm diameter (the same diameter as the inside of the optic mount). The end of the rod was bevelled at 45 degrees, and the mirror and rod combination was spun by hand on the side of a glass cutting saw blade. This process ensured that, when the glass was cut flush with the edge of the rod, the mirror was the correct elliptical shape and diameter to fit in the optics mount. The mirror was then secured to a roughly .5mm thick sheet of indium (to prevent the mirror cracking due to thermal expansion and contraction. This sheet of indium was then epoxied to the mirror mount.

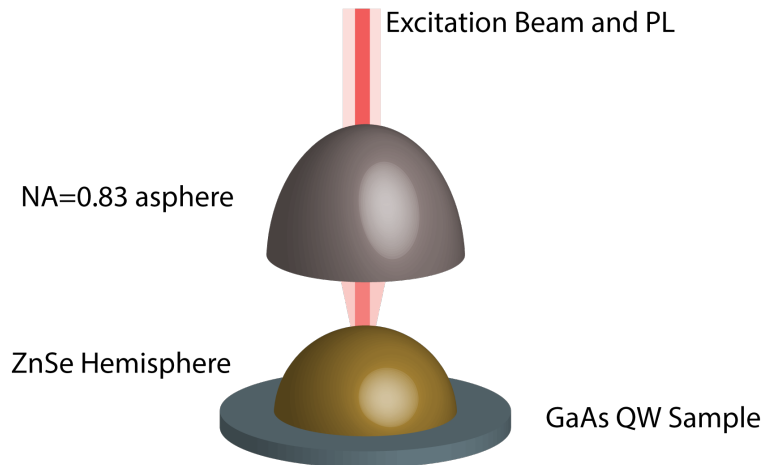


Figure 3.5: A representation of the optics inside the cryostat. The optics were held in place relative to each other by a gold-plated copper mounting tube, containing the lenses. This mounting tube was affixed to a mirror which directed the excitation beam into the cryostat optics and eventually the sample.

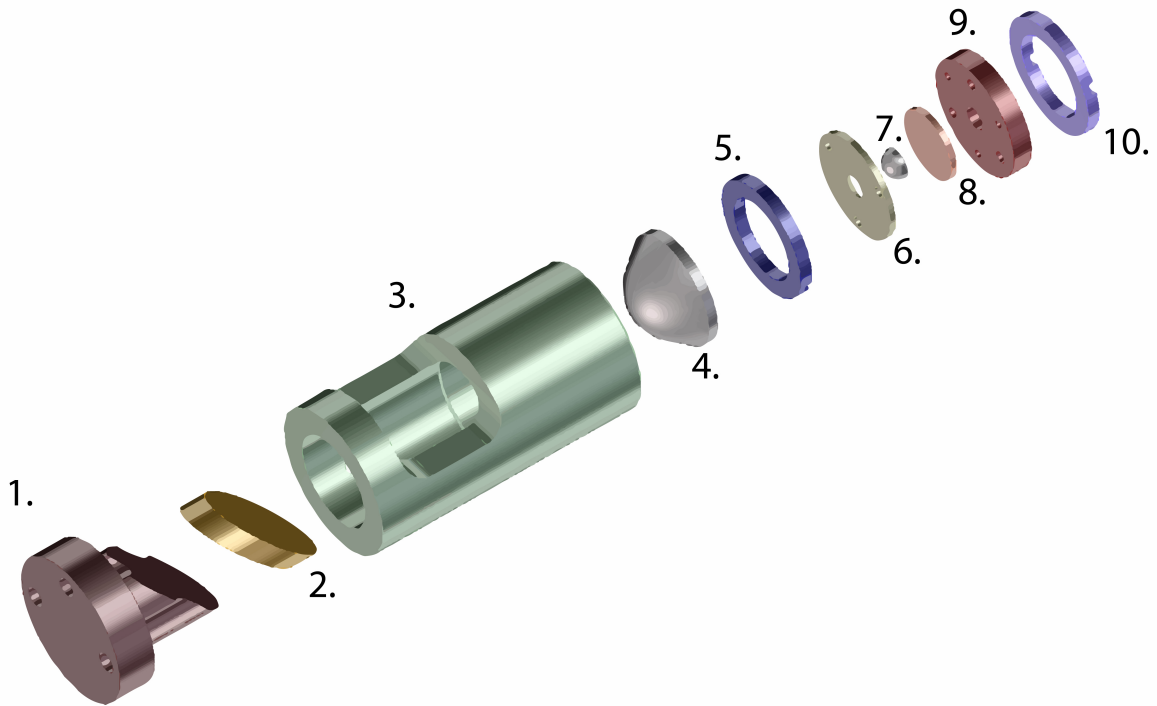


Figure 3.6: An exploded view of the cryostat optical components: 1. the cryostat attachment mount, 2. the cryostat mirror, 3. the copper optics tube, 4. the aspheric lens, 5 the lens retaining ring, 6. the sample and SIL retaining ring, 7. the SIL, 8. the sample, 9. the sample platform, 10. the platform retaining ring. Not rings 5. and 10. were threaded, and the SIL retaining ring clamped onto the sample platform with screws, holding the sample and SIL fixed relative to each other. There was a thin teflon ring between the asphere, the SIL, and their retaining rings to allow for limited thermal expansion and contraction of the lenses without damage.

3.2.3 Experimental Optical Path Configuration

Our aim was to characterize disorder over an area roughly $200\mu\text{m}$ in diameter. In order to do so, we needed the laser spotsize to be $200\mu\text{m}$ in diameter or larger, and we had to collect the PL emitted over this diameter. Additionally, to obtain clear images, the

excitation spot needed to be monotonic, symmetric, and preferably Gaussian in shape. To this end, I characterized the laser spot size and found it to be $1.6 \pm .1\text{mm}$ FWHM diameter, roughly Gaussian and symmetric to within 20%. In order to obtain the requisite beam diameter at the sample, it was necessary to resize the beam going into the cryostat. In order to do so, we used a succession of four lenses to resize the beam. The first two lenses, one of focal length 60mm and the other of focal length 25.4mm, shrunk our beam from 1.6mm to 0.68mm. The second lens in the second pair of lenses was the in-cryostat asphere, and in combination with the lens outside the cryostat, focal length 30mm, resized our beam to $203\mu\text{m}$ in diameter. After the beam hit the sample, the PL signal travelled through the asphere and out of the cryostat. We placed a 90% reflective non-polarizing beamsplitter (NPBS) outside the cryostat to pick off the PL signal. The beamsplitter sent the PL signal through an achromatic, 20cm focal length lens, and a polarizer to filter out the laser. Finally, the signal was then focused onto the slit of a Horiba iHR550 imaging spectrometer with a Horiba Synapse imaging CCD camera. The 20cm lens was 50.4cm in diameter and mounted to a linear translation stage. Its function was to both focus the PL spot on the spectrometer slit and translate the image across the spectrometer slit, as in Figure 3.7. The PL image was roughly 9mm in radius at the lens, so since the lens was relatively large compared to the image, spherical image aberrations during image translation were negligible. We monitored the laser power with a photodiode, using the light that was dumped out of the experiment by the NPBS. Additionally, between the NPBS and the moveable lens, we had the option to add a telescope to improve the magnification of the system further. The use of the telescope depended on the intensity of the signal. If the signal was vanishingly small, the telescope made it nearly unreadable. Therefore, in cases where less signal reached the spectrometer, the telescope became impractical.

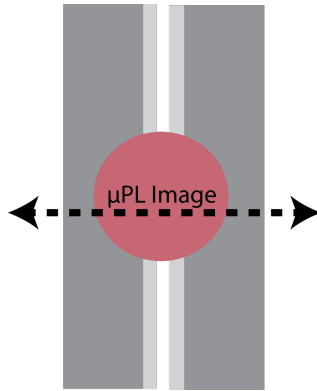


Figure 3.7: A depiction of the PL spot on the spectrometer slit. The spot translates across the slit as we move the lens on the translation stage, allowing us to take vertical slices of the image as it translates across the slit.

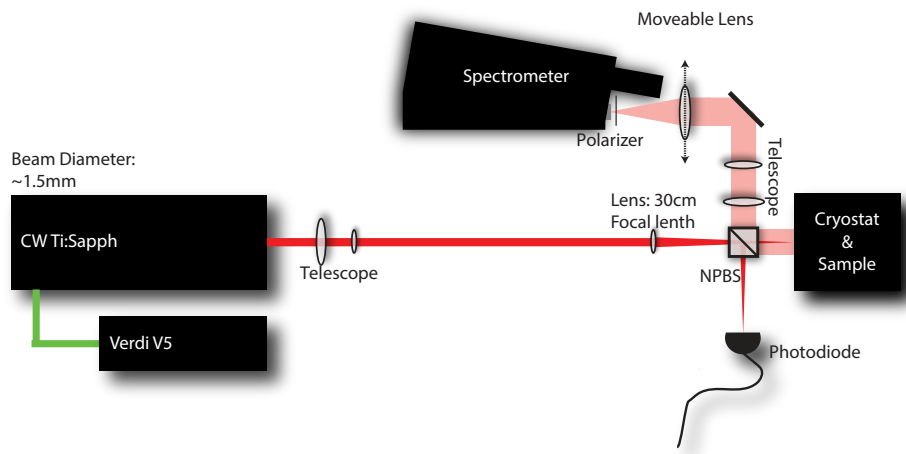


Figure 3.8: A diagram of the experimental components. The second telescope was an optional feature, its use doubled the system magnification. The light pink beam represents the PL image, while the red beam represents the excitation laser.

3.3 μ PL Data Collection

3.3.1 Optical Alignment Considerations

When the optical components were roughly in the configuration seen in Figure 3.8, we cooled the sample to $10 \pm 1\text{K}$ and adjusted the laser power to $10.0 \pm 0.1\text{mW}$ so that the laser power at the sample was roughly 1mW at the sample (because the NPBS dumped 90% of the power we fed into it). We identified the PL signal using a polarization filter, as it was the only signal left after the filter was rotated such that its polarization was orthogonal to that of the beam reflected from the sample. We set the position of the 30cm lens by maximizing the size of the PL image while monitoring it with an IR viewer as we adjusted the position of the lens. Then, we experimentally adjusted the focus of the moveable lens to maximize the spatial differences seen in PL amplitude on the CCD. Finally, we put the polarizer just in front of the spectrometer slit and rotated it to cut out as much laser scatter from the signal as possible.

3.3.2 Data Collection Process

The data collection process was fairly simple. The spectrometer CCD recorded an intensity image 1024×2048 pixels large. The vertical pixel dimension corresponded to vertical spatial dimension on the sample, while the horizontal pixel dimension corresponded to PL emission wavelength and both axes could be calibrated such that we could read peak emission wavelength as a function of vertical sample position. Each image we recorded was effectively a vertical slice of the larger two dimensional PL image. Because we step-translated the PL image across the spectrometer slit and took an image at each lens position, we could recover both PL intensity and PL energy as a function of position. This is exactly the information required to reconstruct a spatial map of QW disorder.

The computer control of the experiment involved five pieces of hardware: two linear actuators, a photodiode, the spectrometer and the imaging CCD. The photodiode was read

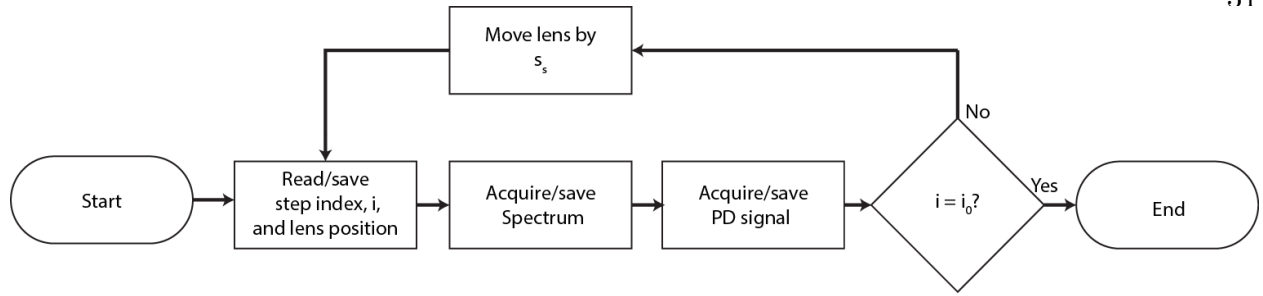


Figure 3.9: A flowchart depicting the LabView code processing sequence. Each set of μ PL data was acquired using this process, where s_s was the lens step size and i_0 was the number of data collection steps to be run.

by the analog-to-digital converter of a Stanford SRS 810 lock-in amplifier using General Purpose Interface Bus (GPIB) protocol. The lens translation stage was actuated by a Newport TRB12 linear actuator, and it was controlled (along with the laser wavelength adjustment) by a Newport ESP300 motion controller interfaced through GPIB. Both the Horiba spectrometer and CCD interfaced over USB. The manufacturers of each of the above devices wrote LabView interface code which I incorporated into my overall experimental control code. The experimental control and data acquisition process proceeded according to the flowchart in Figure 3.9. The collected images and photodiode readings were handled and analyzed with MATLAB code that I wrote.

3.4 Components and Optical Path Configuration for PLE Experiments

3.4.1 Optical Path Configuration and Alignment

Because we didn't need to image the PL from the QW sample in PLE experiments, the optical configuration simplified immensely. The laser first went into an NPBS where about 10% of its power was directed at a photodiode to monitor the laser power during acquisition. From there, the laser travelled to a 7.5cm focusing lens. The lens focused the laser onto our InGaAs/GaAs QW samples, which were rotated at 45 degrees with respect to the laser path

to minimize reflected laser light arriving at the spectrometer. The sample was kept in a Janis STVP-400 helium vapor flow cryostat with tunable temperature control. The PL signal was collected by the same 7.5cm focusing lens, and then sent through a polarizing beam splitter whose polarization was orthogonal to the laser's. Following the beamsplitter, the PL signal was sent to the same achromatic 20cm focal length lens used as the moveable lens in the μ PL experiments. After the lens, the PL signal passed through another polarizer rotated orthogonally to the laser polarization to minimize the laser light entering the spectrometer. The signal then passed into the spectrometer where it was collected as a spectral trace instead of a spectral image. We took data over an area of the CCD which measured 100x2048 pixels. We then integrated over the vertical pixels and recorded spectra which were intensity vs. horizontal pixel number which we calibrated to wavelength. Figure 3.10 is a diagram of the experimental setup. Note, we modified the laser slightly by replacing the output coupler with one coated to work at wavelengths longer than 800nm so we could sweep the laser wavelength out to 850 or 860nm during PLE runs. Only negligible changes to the beamsize and output power resulted from this change.

3.4.2 Data Collection for Photoluminescence Excitation Spectroscopy

The PLE data runs were fairly similar to those used for taking μ PL data. The computer interfaced with the spectrometer, the photodiode, and the laser wavelength actuation in the same way. During the data collection process, we monitored PL intensity as a function of wavelength, recorded these spectra, and then changed the excitation wavelength of the laser. The sets of PLE spectra, BRF actuator position, and PD signal were collected and processed using MATLAB and Igor. Figure 3.11 is a flowchart representing the LabView code I wrote for the data collection process.

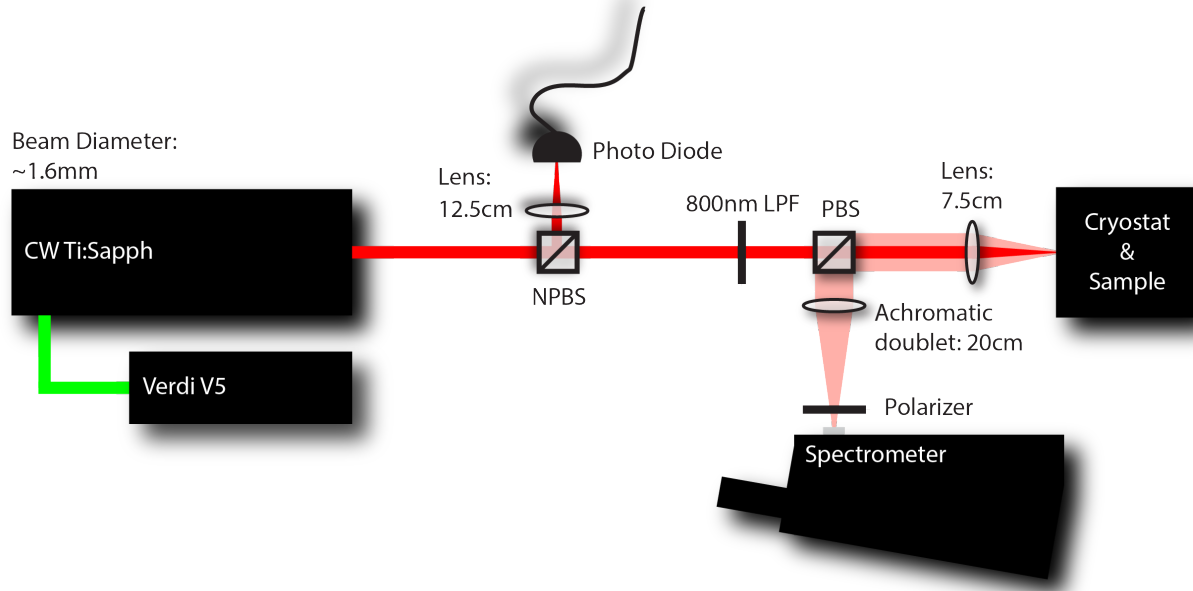


Figure 3.10: A diagrammatic representation of the PLE experiment. The red beam is the excitation laser while the pink beam is the PL signal. We used a long pass filter (LPF) to cut out any light with wavelength lower than 800nm, as we suspected some of the pump scatter (green) was making it to the sample, reducing our ability to control the excitation wavelength.

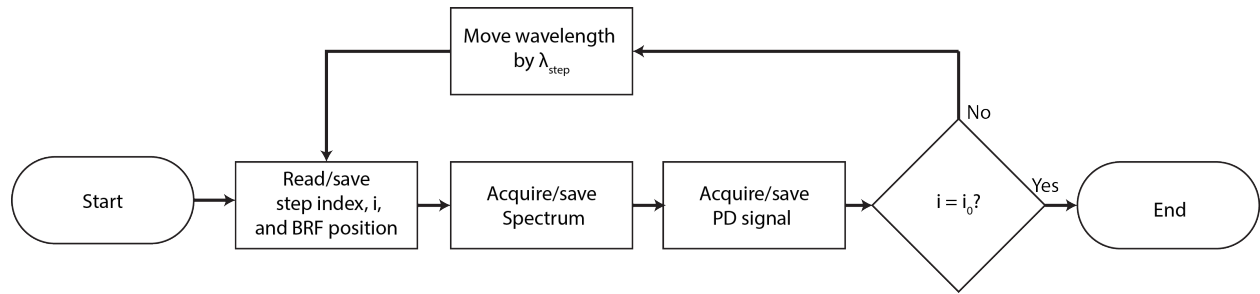


Figure 3.11: A flowchart depicting the LabView code processing sequence for the PLE experiments. Each set of PLE data was acquired using this process, where λ_{step} was the wavelength step size and i_0 was the number of data collection steps to be run.

Chapter 4

Disorder in Quantum Well Structures

4.1 μ PL Results and Analysis for Multiple Quantum Well Samples

4.1.1 Disorder in a Ten Quantum Well Structure

As a proof-of-concept test for our μ PL experiment, we decided to measure the structural disorder in a ten-period 10nm GaAs QWs. Note: for the following discussion, the ten-period QW and the four-period QW samples will be referred to as the 10QW and 4QW samples respectively. We expected to see a large PL signal from this sample. Therefore, it was our goal to measure a PL image of the 10QW sample, with our laser exciting near-resonantly. The excitation wavelength was 773nm, while the detection center wavelength was 812nm, and the PL signal peaked around 808nm. Figure 4.1 shows a single raw image corresponding to a vertical slice of the total PL image.

From the raw spectrometer images, we found the wavelength corresponding to the maximum PL amplitude at each vertical row of CCD and read that pixel's PL wavelength and amplitude information. We then compiled that information into either a PL amplitude or PL energy vector corresponding to the lens position. Effectively, at each lens position, we took a vertical slice of the raw image and stacked that information along the lens translation direction to obtain a 2D image. Figure 4.2 shows a representative vertical image slice from the images taken on the 10QW sample. From this, we took the peak PL amplitude from each lens position and stacked it into a PL image. A representative image, from the 10QW sample can be seen in Figure 4.3. The structures in the PL image correspond to artifacts

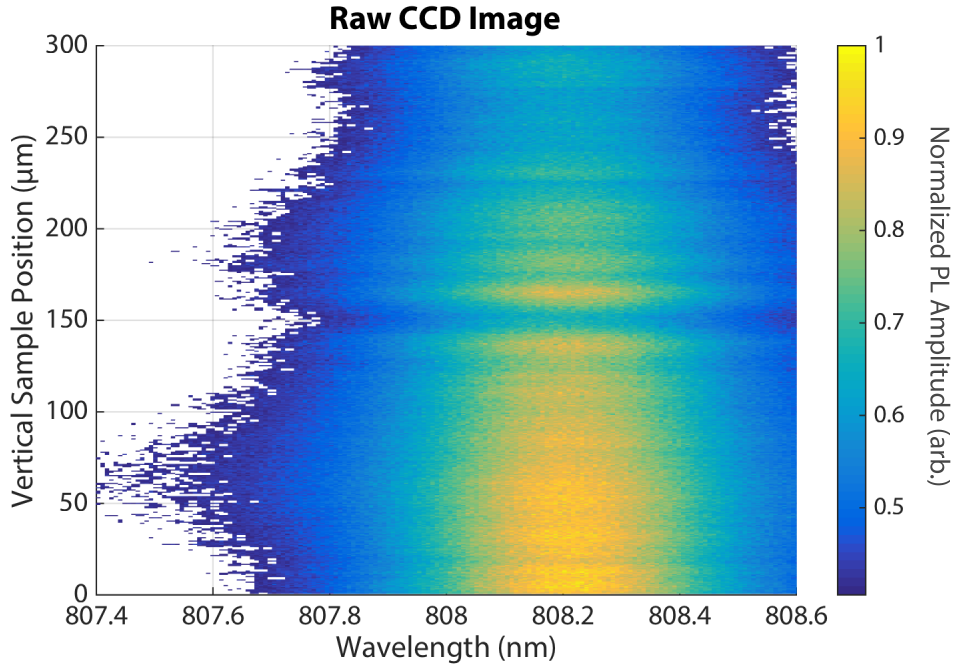


Figure 4.1: A raw CCD image corresponding to one vertical slice of the PL image. In order to calculate the PL emission wavelength as a function of sample location, we found the maximum PL amplitude as a function of vertical sample position for each vertical slice.

on the surface of the QW sample: despite our best efforts, surface imperfections and dust were present on the sample during data runs. However, the fact that we are actually able to produce a PL image reconstruction which shows the imperfections as defined reductions in PL signal indicates that the sample surface was in focus, and we are near the maximum image definition we can expect for the disorder map.

From this image, we can estimate the resolution limit for the PL image alone. Doing so, we calculated that the resolution limit for our imaging system was limited by the repeatability of the lens position, $0.5\mu\text{m}$, which corresponds to 225nm at the sample surface, while we stepped the lens by slightly less than the repeatability, $0.4\mu\text{m}$, to be sure that the repeatability was the limiting factor for our horizontal resolution. We were limited in the vertical direction by the camera pixel size, which was $13.6\mu\text{m}$. Because our magnification

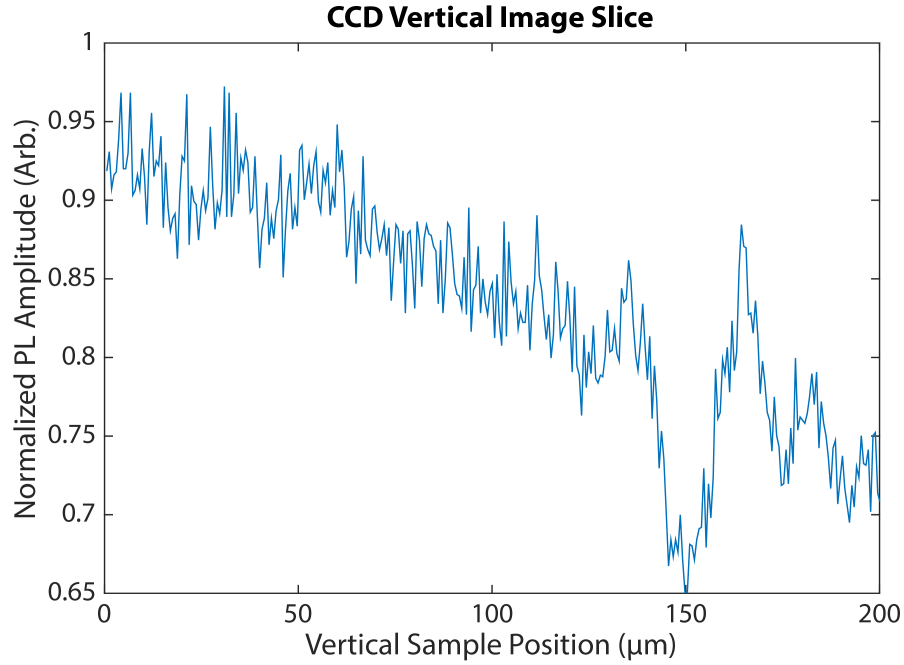


Figure 4.2: A vertical 10QW PL amplitude slice at the PL maximum from a CCD raw image. Effectively, these slices were stacked together along the lens translation axis to recover the second sample location axis and build a 3D surface of either PL amplitude or PL energy.

factor was 22.22x, our vertical resolution was no better than 612nm on the sample. This was not our goal of 185nm; however, one can ameliorate this issue by inserting a telescope, with 2x magnification, between the NPBS and the achromatic doublet. An unfortunate side effect of increased resolution, however, was decreased signal strength. It was therefore necessary to increase CCD integration time or increase PL emission by increasing excitation power, but as we were exciting the sample with an already relatively high power of 1mW, increasing the resolution necessitated increasing integration time. For the 4QW sample, we took data with the telescope in place, but for the 10QW sample, a resolution of 225.0x612.0nm was the best we achieved.

Though our resolution was less than optimal, we were still able to calculate an energy deviation map for the 10QW sample. To do this, we found the emission energy corresponding

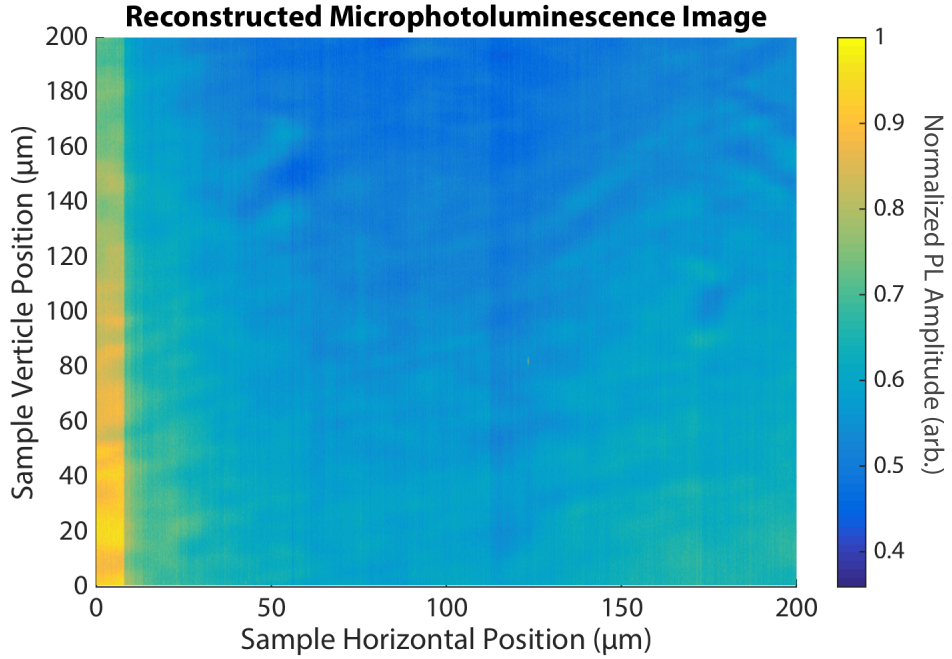


Figure 4.3: A reconstructed PL image of 10QW sample surface. The small features in the image correspond to striations and dust on the surface of the sample. The excitation spot's maximum intensity occurred near the bottom of the image, corresponding to the PL amplitude maximum.

to the maximum PL amplitude at each vertical pixel. We then stacked each of these points (for which we had an energy vs. vertical sample position vector) along the horizontal image axis at each lens position. Once done, we then calculated the average PL energy for the entire PL image. Then, we found the local energy deviation from the average PL energy by subtracting the average PL energy from the local PL energy. Simply:

$$\delta E_{i,j} = E_{i,j} - E_{avg} \quad (4.1)$$

where E_{avg} is the average emission energy for the whole PL picture, and i, j index horizontal and vertical sample position respectively. Following this, we obtain our μ PL map. However, this map is too noisy to see structure, as CCD intensity fluctuations of roughly 10 counts or 1% of the total signal will affect PL peak amplitude location on the CCD, and thus the peak

energy at a given sample location. Therefore, we must take our μ PL energy deviation map and Gaussian smooth the energy deviation values by two to five pixels FWHM depending on the sample. Doing so, we obtain the energy deviation map seen in Figure 4.4. This, however, reduces our resolution further, as adjacent pixels now carry information about the average value of pixels around them. Our horizontal resolution for the deviation map, as measured on the deviation image by looking at closest distinguishable pixels, is now 360nm. Note: since we had much many more horizontal image slices than vertical pixels, the effect of the Gaussian blur on reduced resolution seemed to be more prominent in the horizontal direction. Therefore, even though adjacent pixels were still distinguishable in the vertical direction, our vertical resolution was now between 612nm and 800nm.

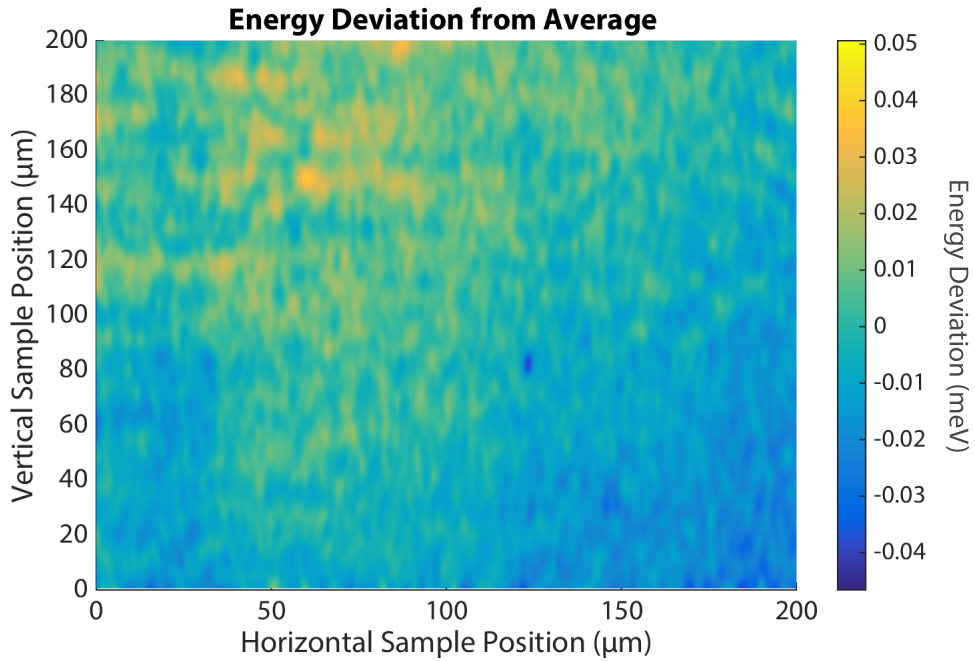


Figure 4.4: A μ PL energy deviation image for the 10QW sample. Note the energy deviation was found to be 0.1meV, peak to peak, at maximum.

We expected energy deviations as a result of QW width fluctuations to behave according to the following equation:

$$\delta E = \frac{h^2\pi^2}{2\mu_{HH}} \left(\frac{1}{(L^* \pm a)^2} - \frac{1}{L^{*2}} \right) \quad (4.2)$$

where δE is the PL energy deviation due to a well width fluctuation of $\pm a$, μ_{HH} is the heavy-hole reduced mass, and $L^* = L + 2\delta$ is the effective well width accounting for electron wave-function penetration of 15Å into the AlGaAs barrier, and $\mu_{HH} = 0.055m_e$ is the reduced exciton mass [10, 17]. We saw energy deviations of about ??meVpp, which was five times less than expected. This discrepancy was due for the most part to signal averaging within the 10QW sample PL image: the relatively weak PL signal from spots in the wells which deviated from average width was most likely from the first few wells, and not all 10QWs. Additionally, since we looked only at the maximum amplitude PL signal from each point in the sample, due to the random distribution of disorder, the maximum PL energies at each PL image location would tend to be close to the average PL energy for the whole sample, as the signal at each location was presumably an average over the QW emission from each well at each imaging location. In other words: the way we took our PL image meant that any disorder deviations we saw would be due to the additive effects of disorder over multiple wells, meaning that disorder fluctuations were smaller than expected in the one QW limit. Using Equation 4.2, we expect energy deviations of roughly 0.5meV for disorder variations of one crystal monolayer. Anything less than this corresponds to no measured well width variations whatsoever. However, we do measure energy deviations in our μ PL images. What we are measuring is the averaged width fluctuations over a number of quantum wells, not width fluctuations for just one well.

4.1.2 Disorder in a Four Quantum Well Structure

Because the 10QW PL energy deviations due disorder were fairly small, we decided to take μ PL data on a four-period 10nm GaAs QW with 10nm AlGaAs barriers. As 4QW

sample had fewer wells, but each was identical in width to the 10QW sample, we expected to see larger disorder energy deviations because there would be fewer wells over which the signal would be averaged. Additionally, we inserted a telescope into the PL imaging path, increasing our on-sample resolution. In the horizontal direction, the resolution limit was no longer set by the lens translation. Rather, since we were able to magnify our image by 2x, the horizontal resolution was diffraction limited to 192.9 ± 0.3 nm, as our PL wavelength peaked around 807.8nm, with a FWHM of 0.6nm. The vertical resolution was increased by a factor of two from 612.0nm to 306.0nm. Therefore, for the 4QW sample, our on-sample resolution was theoretically 192.9x306.0nm. This is close to our goal of a completely diffraction-limited system, but we still weren't quite able to achieve that in the vertical imaging direction. However, again the energy deviation map data was quite noisy. As a result, we Gaussian smoothed the data with a FWHM of 2px at each data point. Therefore, though our PL image had a resolution of 192.9x306.0, our energy 4QW map was limited to a resolution of 252x400nm. Figure 4.5 is a reconstructed PL image collected from the 4QW sample, while figure 4.6 is the image deviation map corresponding to the PL image.

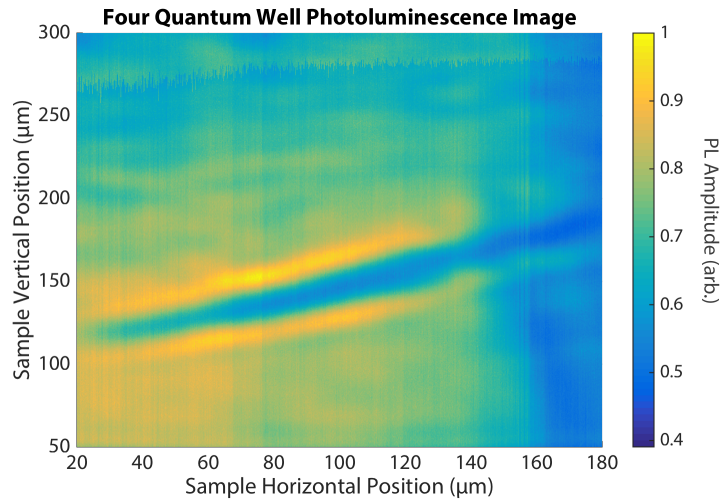


Figure 4.5: A reconstructed image of the PL amplitude of the 4QW sample.

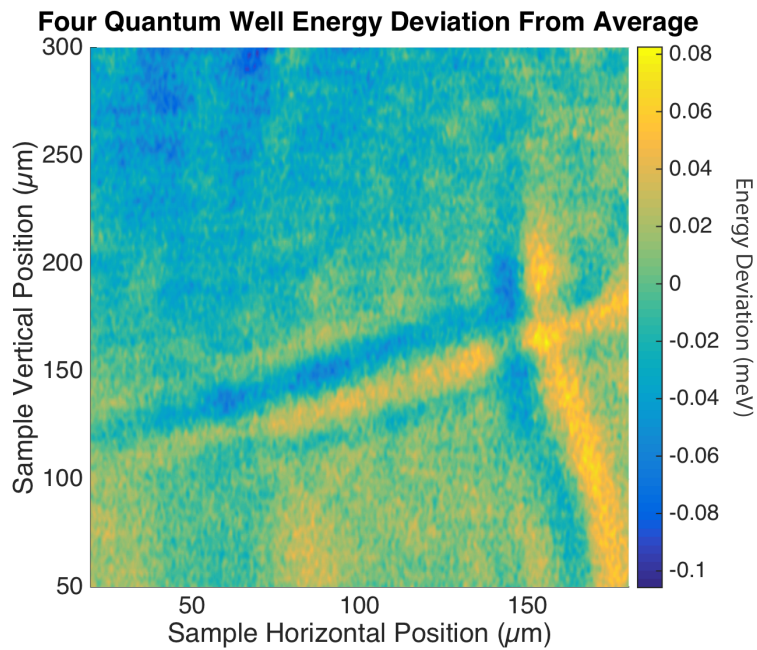


Figure 4.6: An energy deviation map for the 4QW sample. Note the large-scale feature across the middle of the sample. This most likely corresponded to a scratch across the sample which slightly deformed all four wells below it, so we see an energy signature of this deformation.

With the periodic 4QW structure, we were still running into the same problems we had with the 10QW sample: due to spectral averaging over multiple quantum wells, we saw energy deviations corresponding to well width variations of less than a monolayer. Though the energy deviations from disorder for each single quantum well were presumably larger than those we saw, we weren't able to resolve the disorder variations in just one quantum well.

4.1.3 Disorder in an Interfacial Quantum Dot Structure

Our final disorder measurement was taken on an interfacial quantum dot (IQD) sample. Due to high signal averaging for the MQW samples, we weren't able to see the energy deviations we theoretically should have. Subsequently, we took μ PL data on a 5-period, varying well and barrier thickness GaAs/AlGaAs quantum well. Due to the growth process of the IQD sample, smaller well widths and similar width fluctuations translate to three-dimensional exciton confinement [15, 8], rather than just the one QW confinement dimension. Though the sample was a five-period structure, there was less spectral averaging than the 10QW and 4QW samples. This is clear in Figure 4.7. Additionally, due to the smaller well width for some of the IQD wells relative to the other two QW samples, our original light source was slightly unreliable at the shorter wavelengths necessary to probe IQD disorder: as we tuned the Ti:Sapph laser below 750nm, it would occasionally enter multi-mode operation. When this occurred, the laser would operate at diminished and unstable power. We therefore used a green laser, centered at 532.15nm to excite the IQD sample.

From these measurements, we were able to calculate a maximum PL energy deviation of 0.74meV, peak to peak. This value was larger (and much more representative of PL energy fluctuations caused by disorder) than that for 10QW and 4QW structures. Therefore, we were able to measure well width variations greater than one monolayer in the IQD sample. Though there was still spectral averaging due to the fact that the IQD sample was five wells thick, this was due to the diversity of well widths present in the IQD sample by design.

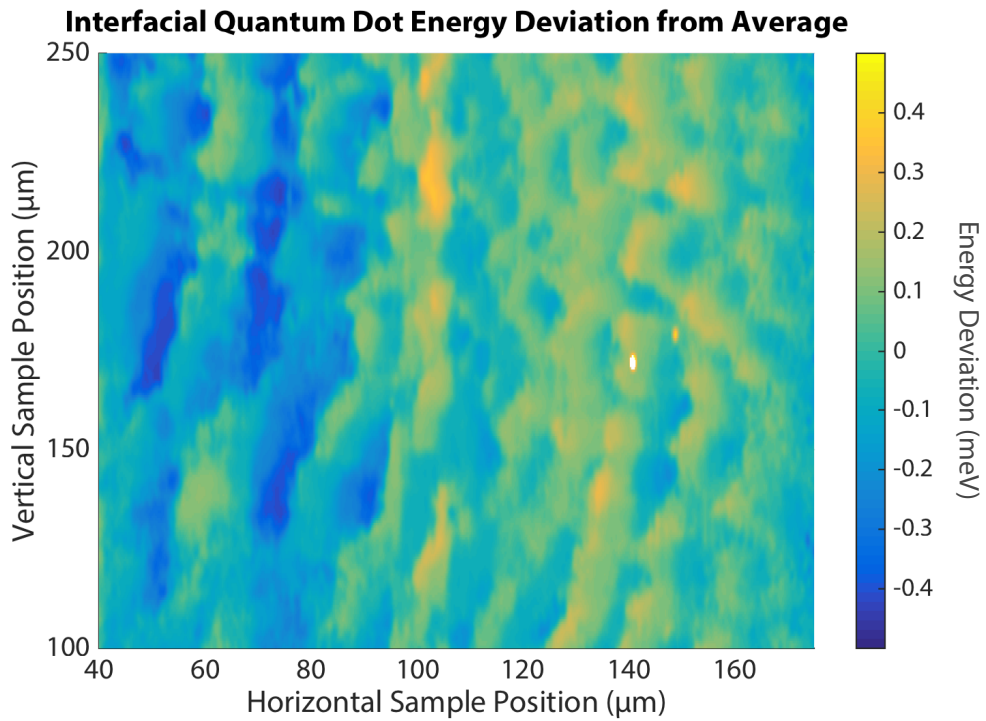


Figure 4.7: An energy deviation map for the IQD sample. The energy deviations in the IQD sample are much larger than those measured in the 4QW and 10QW samples, even though the IQD structure is periodic and suffers from similar spectral averaging to the other samples. The white blemish is an anomalous noise spike.

4.2 PLE Results and Analysis

For our asymmetric double quantum well samples, we had InGaAs wells of 9nm and 10nm thickness with a GaAs barrier between them. We had three samples of varying barrier thickness, b , with $b = 5, 10$, or 30nm . For each sample, we excited with our CW laser, and collected PL from the sample. We then stepped our laser excitation wavelength and monitored the PL spectra as a function of CW excitation wavelength. We found in each case that there was incoherent Stokes- and anti-Stokes coupling of excitons between wells. Figure 4.9 shows a close-up of the coupling peaks, while Figure 4.8 shows an example PLE spectrum for an AQW sample with a barrier width of 10nm.

Traditionally, PLE is done by monitoring emission intensity at a single wavelength [3], but with our experiment, we are able to measure a full spectrum at each excitation wavelength. This ability means that our PLE spectra are more rich, as they provide simultaneous information of both narrow and wide well emission. Taking vertical slices along the emission peaks from the narrow and wide wells, we obtain information on exciton population by monitoring the emission amplitudes. We can then plot PLE emission amplitude as a function of excitation wavelength and monitor the strength of the Stokes- and anti-Stokes cross peaks as well as other peaks in emission corresponding to exciton ground and excited state emission. Figure 4.10 is an assembly of vertical PLE slices for three PLE spectra recorded at 10K. Note: as the barrier width decreases, the strength of the Stokes- and anti-Stokes peaks increases.

Figure 4.10 shows increased coupling between wells as barrier width decreases: both the red dashed trace peak around 1.46eV and the blue trace peak around 1.47eV increase as barrier width decreases. We measure, then, what we expect qualitatively: as AQWs get closer together, the incoherent coupling between excitons in each well increases. However, we were initially surprised that we measured coupling in the anti-Stokes direction. Intuitively, one would expect that an exciton in the wider well, because it exists at a slightly lower energy,

would not be able to emit from a state in the narrower well. We suspected, therefore, that coupling in the anti-Stokes direction would be a temperature mediated process. As a result, we took PLE data on all three barrier sizes and monitored the cross-peak intensity as a function of temperature. Figure 4.11 shows that the coupling between wells seems to be a temperature mediated process in the 10nm and 30nm barrier samples. However, in the 5nm barrier sample, the temperature dependance of coupling seems to be vanishingly small if any, likely because the barrier acts more like a perturbation to the exciton ground state than a true well barrier. In the lower set of figures, the cross-peak intensity is normalized to the resonant peak intensity by measuring the wings of the resonant peak at three locations: on resonance, and at slightly lower and higher detection frequencies. Then, because the resonant peak was obscured by the laser scatter signal, we estimate the hight of the resonant peak using the shape and intensity of the peak wings. We then use the estimated resonant peak height to normalize the cross-peaks so we can compare the height of the cross-peaks to the height of the resonant peaks and comment on the coupling emission intensity relative to the resonant emission intensity. Others have seen similar temperature-dependence of coupling in the anti-Stokes direction, [3] but have failed to provide a model that accounts for the intensity of the coupling peaks as a function of temperature and of barrier width.

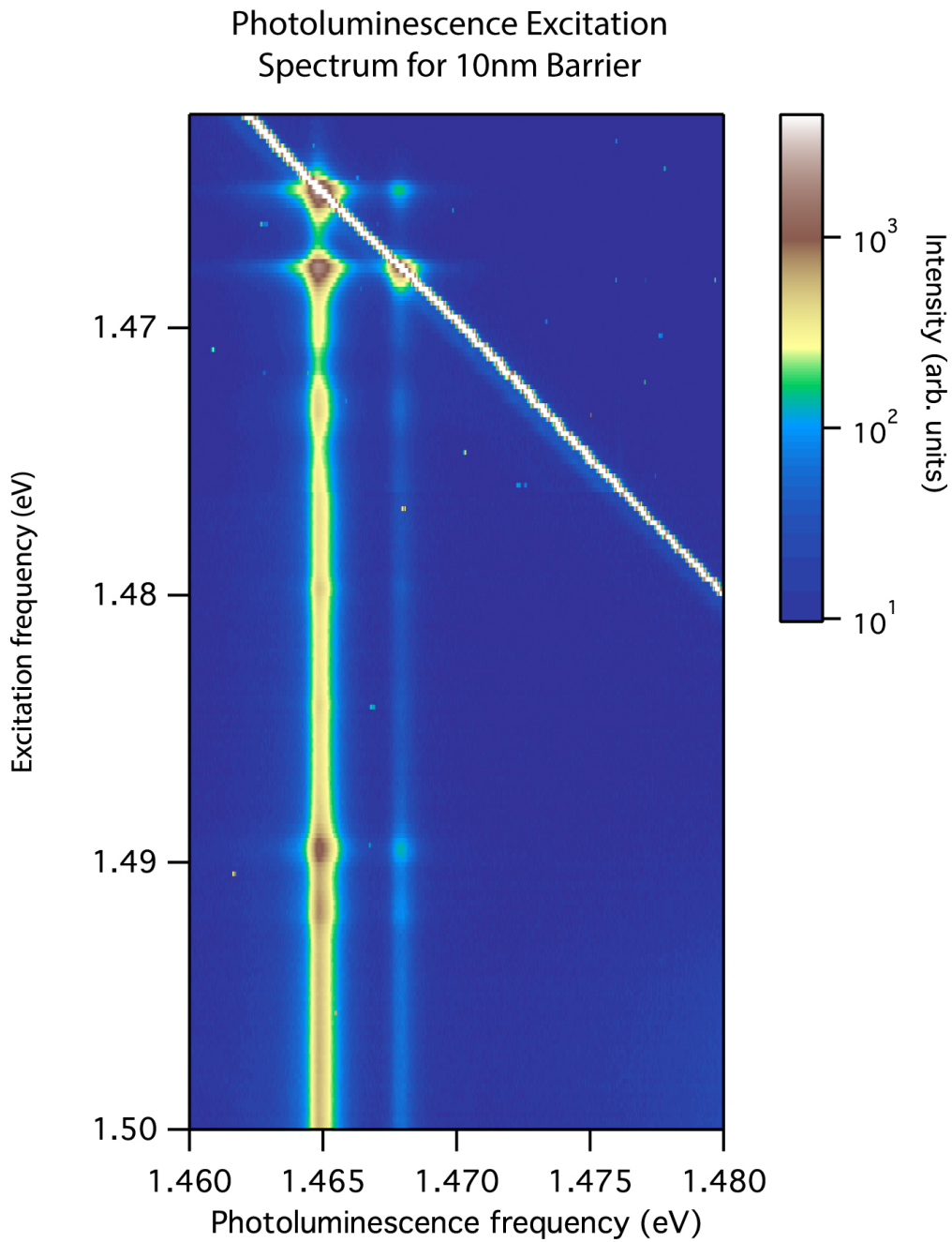


Figure 4.8: An example PLE spectrum taken on a 10nm barrier AQW sample. We were able to monitor the emission from both wells as a function of excitation frequency, which allowed us to simultaneously quantify emission from one well due to resonant excitation and emission from the adjacent well due to coupling. The lower energy vertical trace corresponds to emission from the wide well while the higher energy trace corresponds to emission from the narrow well. The white diagonal line is laser scatter, and represents locations of equal excitation and detection frequencies.

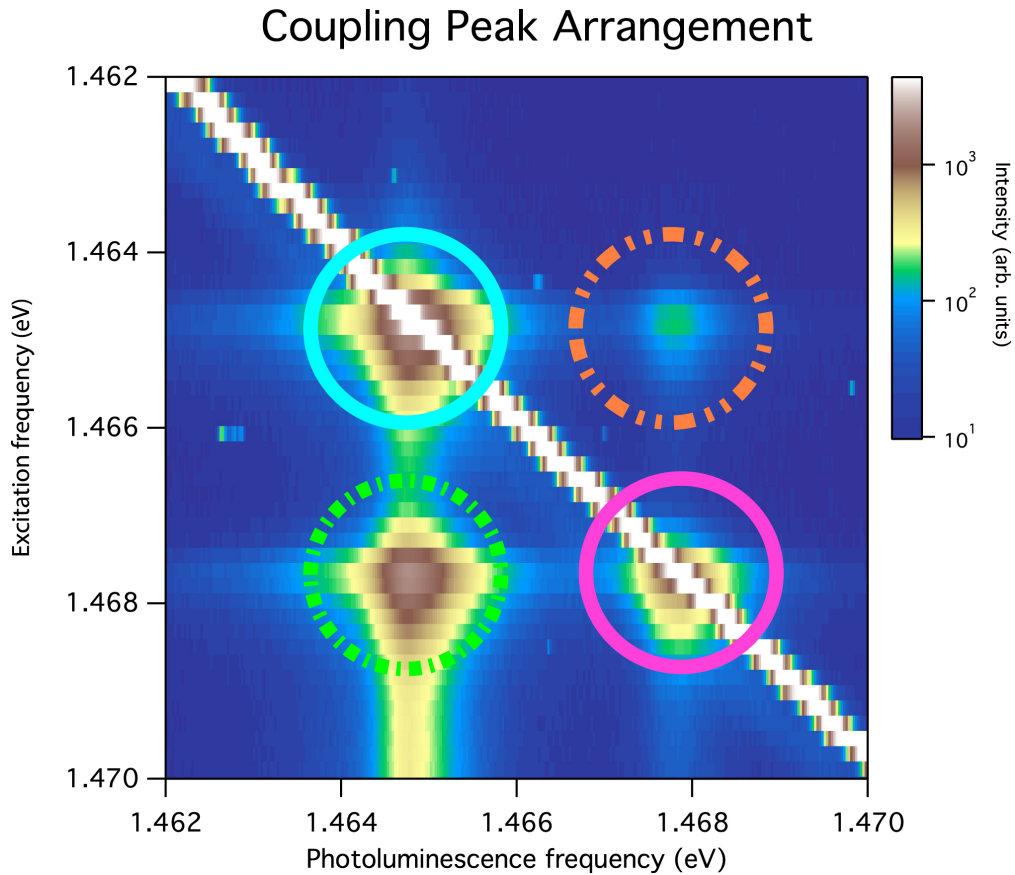


Figure 4.9: A close-up of the coupling cross-peaks. The green, dashed circle corresponds to a coupling peak between wells in the Stokes direction: the narrow well absorbs the laser excitation, while the wide wells emit a portion of the absorbed energy. The orange, dashed circle corresponds to a coupling peak in the anti-Stokes direction: the wide well absorbs and the narrow well emits a portion of the excitation energy. The magenta circle corresponds to resonant excitation in the narrow well, and the turquoise circle corresponds to resonant excitation in the wide well. The diagonal white trace is the laser scatter.

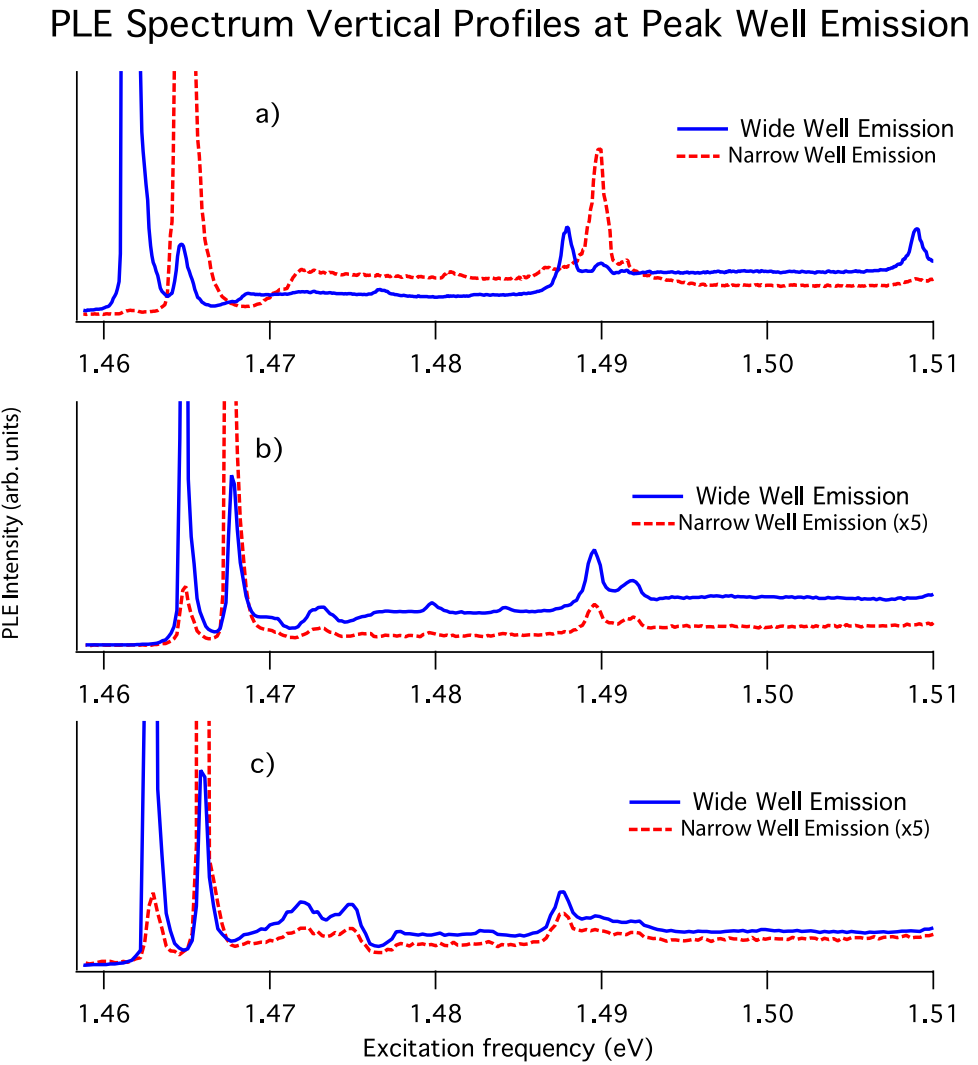


Figure 4.10: A set of three PLE vertical profiles taken at the wavelength of peak emission intensity for a) the 30nm, b) the 10nm, and c) the 5nm barrier width AQW. Note: the narrow well emission intensity was much lower than the wide well emission intensity, and was scaled up for graphical comparison. For each sample, the most intense peaks correspond to resonant excitation and absorption. The coupling intensity can be measured by looking at the intensity of the cross peaks, represented by the slightly smaller peaks under each of the resonant excitation peaks.

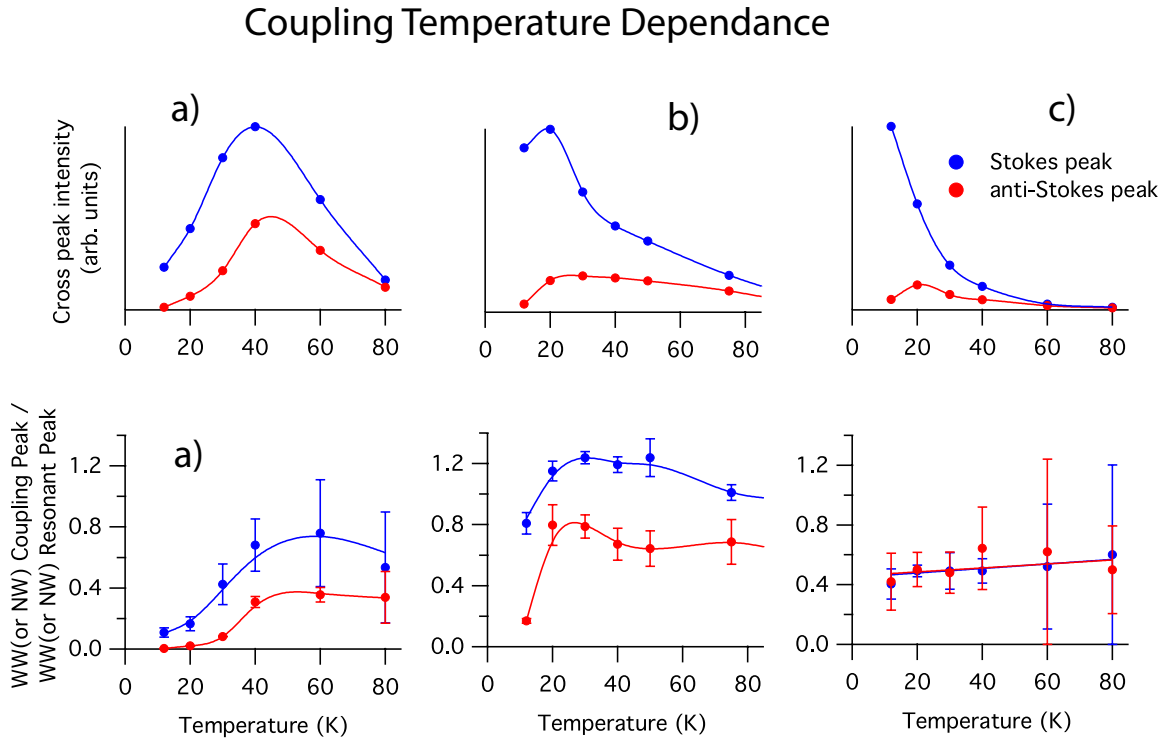


Figure 4.11: Temperature dependance for the PLE coupling peaks for barrier width of a) 30nm, b) 10nm, and c) 5nm. The top plots are un-normalized coupling peak intensities, while in the bottom plots, the cross-peak intensity is normalized to the resonant peak intensity. The coupling intensity seems to have a temperature peak for the 30nm and 10nm barrier samples. The coupling peak intensities in both the normalized and unnormalized plots for these two samples decrease as sample temperature increases, suggesting that coupling is temperature mediated. However, in the 5nm barrier, there seems to be little temperature dependance of coupling intensity in the normalized plot.

Chapter 5

Conclusion and Future Work

5.1 Conclusions from Linear Spectroscopic Experiments

In this thesis I've presented the development of a way to obtain a spatial and spectral picture of semiconductor quantum well disorder. I have shown, furthermore, that we can obtain the desired quantification of disorder for a variety of QW systems. However, due to spectral averaging, this method is unable to distinguish the disorder contributions from individual wells in MQW samples. This was to be expected, however, as over more than two quantum wells, the disorder effects on PL energies smear out and have the effect of broadening PL line-widths.

In more disordered systems, like IQDs, μ PL provides a unique way to measure spatial disorder. When the effects of spectral imaging can be minimized, such as in our IQD samples or in single QW samples, this method can provide adequate spatial resolution to resolve the effects of disorder on PL emission energies at the small disorder size scales.

Taken as a whole: I showed, with the data taken on the 4QW system, that with a sufficiently high magnification, it is possible to achieve the spatial resolution necessary to image structural disorder. Furthermore, with the data taken on the IQD system, I showed that our method has the ability to provide a spectrally resolved picture of PL emission. Therefore, with the correct samples (highly disordered QWs or presumably single QWs), we can use this method successfully to quantify structural disorder in semiconductor nanostructures.

I showed that incoherent coupling between AQW excitons can be studied in detail with

our enhanced PLE measurements. The richness of the data we retrieve using a spectrometer allows us study coupling in both the Stokes and anti-Stokes directions simultaneously. When employed to study the temperature dependance and barrier width dependance of incoherent coupling between QW excitons, we showed that our enhanced PLE technique is capable of producing a wealth of data about coupling strength and PL line-shapes that otherwise would not be possible.

5.2 Future Work

A natural next step for the μ PL experiments we conducted would be to study single quantum well samples to see if we can, as in the case with IQDs, extract adequate spatial and spectral data from the PL signal to quantify the disorder of a single well, as that result is more easily generalizable than the IQD μ PL result. Additionally, it would be useful to combine μ PL data taken, on MQW or other QW samples, with two-dimensional Fourier transform spectroscopy taken on the same samples to see how localization and disorder affect the nonlinear optical response of QW excitons.

Our PLE studies of AQW systems proved useful in locating exciton states and quantifying incoherent coupling between exciton states in the adjacent wells. We could further our understanding of incoherent coupling by developing a better understanding for thermal mediation of coupling that adequately treats both temperature and barrier width dependance, as authors have independently addressed those questions in the past [3, 2, 19].

References

- [1] Refractive index of ZnSe (Zinc selenide) - Connolly.
- [2] M. Batsch, T. Meier, P. Thomas, M. Lindberg, S. W. Koch, and J. Shah. Dipole-dipole coupling of excitons in double quantum wells. Physical Review B, 48(16):11817, 1993.
- [3] P. Borri, M. Guriolo, M. Colocci, A. Patanè, M. Grassi Alessi, M. Capizzi, and F. Martelli. Carrier transfer between ingaas/gaas quantum wells separated by thick barriers. physica status solidi (a), 164(1):227–230, 1997.
- [4] A. D. Bristow, T. Zhang, M. E. Siemens, S. T. Cundiff, and R. P. Mirin. Separating Homogeneous and Inhomogeneous Line Widths of Heavy- and Light-Hole Excitons in Weakly Disordered Semiconductor Quantum Wells. The Journal of Physical Chemistry B, 115(18):5365–5371, May 2011.
- [5] F. F. Chen and F. F. Chen. Introduction to plasma physics and controlled fusion. Plenum Press, New York, 2nd ed edition, 1984.
- [6] S. T. Cundiff. Optical two-dimensional Fourier transform spectroscopy of semiconductor nanostructures [Invited]. JOSA B, 29(2):A69–A81, 2012.
- [7] J. H. Davies. The physics of low-dimensional semiconductors: An introduction. Cambridge University Press, 1998.
- [8] M. Fox. Optical properties of solids. Oxford master series in condensed matter physics. Oxford University Press, Oxford ; New York, 2001.
- [9] M. A. Gilleo, P. T. Bailey, and D. E. Hill. Free-Carrier and Exciton Recombination Radiation in GaAs. Physical Review, 174(3):898, 1968.
- [10] Y. D. Glinka, Z. Sun, M. Erementchouk, M. N. Leuenberger, A. D. Bristow, S. T. Cundiff, A. S. Bracker, and X. Li. Coherent coupling between exciton resonances governed by the disorder potential. Physical Review B, 88(7), Aug. 2013.
- [11] D. Griffiths. Introduction to Quantum Mechanics. Pearson, 2 edition, 2005.
- [12] J. Hegarty, L. Goldner, and M. D. Sturge. Localized and delocalized two-dimensional excitons in GaAs-AlGaAs multiple-quantum-well structures. Physical Review B, 30(12):7346, 1984.

- [13] G. Iadonisi, G. Cantele, and M. L. Chiofalo. Introduction to Solid State Physics and Crystalline Nanostructures. Springer, 2014.
- [14] D. A. Miller. Optical physics of quantum wells. Quantum Dynamics of Simple Systems,” ed. G.-L. Oppo, SM Barnett, E. Riis, and M. Wilkinson (Institute of Physics, London, 1996), pages 239–266, 1996.
- [15] G. Moody. Confinement Effects on the Electronic and Optical Properties of Semiconductor Quantum Dots Revealed with Two-Dimensional Coherent Spectroscopy. PhD thesis, University of Colorado, Boulder, 2013.
- [16] J. Patterson and B. Bailey. Solid-State Physics. Springer Berlin Heidelberg, Berlin, Heidelberg, 2010.
- [17] P. V. Santos, M. Willatzen, M. Cardona, and A. Cantarero. Tight-binding calculation of spin splittings in semiconductor superlattices. Physical Review B, 51(8):5121–5129, Feb. 1995.
- [18] D. B. Sirdeshmukh, L. Sirdeshmukh, K. G. Subhadra, and C. S. Sunandana. Electrical, Electronic and Magnetic Properties of Solids, volume 207 of Springer Series in Materials Science. Springer International Publishing, Cham, 2014.
- [19] A. Tomita, J. Shah, and R. S. Knox. Efficient exciton energy transfer between widely separated quantum wells at low temperatures. Physical Review B, 53(16):10793, 1996.
- [20] unk. Titan-CW Ti:sapphire laser Operation Manual. Technical report, Schwartz Electro-optics.
- [21] C. Weisbuch, R. Dingle, A. Gossard, and W. Wiegmann. Optical characterization of interface disorder in gaas-ga_{1-x}al_xas multi-quantum well structures. Solid State Communications, 38(8):709 – 712, 1981.
- [22] M. Yoshita, N. Kondo, H. Sakaki, M. Baba, and H. Akiyama. Large terrace formation and modulated electronic states in (110) GaAs quantum wells. Physical Review B, 63(7), Jan. 2001.
- [23] M. Yoshita, T. Sasaki, M. Baba, and H. Akiyama. Application of solid immersion lens to high-spatial resolution photoluminescence imaging of GaAs quantum wells at low temperatures. Applied Physics Letters, 73(5):635, 1998.